

11-21-2022

Characteristics of Kelvin-Helmholtz Waves as Observed by the MMS from September 2015 to June 2017

Katariina Nykyri

Embry-Riddle Aeronautical University, nykyrik@erau.edu

Xuanye Ma

Embry-Riddle Aeronautical University, max@erau.edu

Rachel C. Rice

Embry-Riddle Aeronautical University, RICER4@my.erau.edu

Follow this and additional works at: <https://commons.erau.edu/publication>



Part of the [Astrophysics and Astronomy Commons](#)

Scholarly Commons Citation

Nykyri, K., Ma, X., & Rice, R. C. (2022). Characteristics of Kelvin-Helmholtz Waves as Observed by the MMS from September 2015 to June 2017. *JGR Space Physics*, (). <https://doi.org/10.1002/essoar.10503472.1>

This Article is brought to you for free and open access by Scholarly Commons. It has been accepted for inclusion in Publications by an authorized administrator of Scholarly Commons. For more information, please contact commons@erau.edu.

Characteristics of Kelvin-Helmholtz Waves as Observed by the MMS from September 2015 to June 2017

Rachel C Rice¹, Katariina Nykyri¹, and Xuanye Ma¹

¹Embry-Riddle Aeronautical University

November 21, 2022

Abstract

The Magnetospheric Multiscale (MMS) mission has presented a new opportunity to study the fine scale structures and phenomena of Earth's magnetosphere, including cross scale processes associated with the Kelvin-Helmholtz Instability (KHI). We present an overview of 19 MMS observations of the KHI from September 2015 to June 2017. Unitless growth rates and unstable solid angles for each of the 19 events were calculated using 5 techniques to automatically detect plasma regions on either side of the magnetopause boundary. There was no apparent correlation between solar wind conditions during the KHI and its growth rate and unstable solid angle, though we note no KHI were observed for solar wind flow speeds less than 300 km/s or greater than 600 km/s, likely due to a filtering effect of the instability onset criteria and plasma compressibility. Two-dimensional Magnetohydrodynamic (2D MHD) simulations were compared with two of the observed MMS events. Comparison of the observations with the 2D MHD simulations indicates that velocity dependent methods are the most consistent when calculating growth rate and unstable solid angle, but a combination of the velocity dependent and independent methods can be used to select KHI events in which the vortex has rolled over. This may prove useful for future work studying secondary processes associated with the KHI.

1 **Characteristics of Kelvin-Helmholtz Waves as Observed**
2 **by the MMS from September 2015 to June 2017**

3 **Rachel Rice¹, Katariina Nykyri¹, Xuanye Ma¹**

4 ¹Embry-Riddle Aeronautical University, Department of Physical Sciences, Center for Space and
5 Atmospheric Research

6 **Key Points:**

- 7 • A survey of MMS data from September 2015 to June 2017 identified 19 Kelvin-
8 Helmholtz wave events.
- 9 • KH events are only observed for solar wind speed between 300–600 km/s. KHI
10 growth rates are otherwise independent of solar wind conditions.
- 11 • New methods are developed for the automatic detection of magnetosheath and mag-
12 netospheric regions within the KHI.

Abstract

The Magnetospheric Multiscale (MMS) mission has presented a new opportunity to study the fine scale structures and phenomena of Earth’s magnetosphere, including cross scale processes associated with the Kelvin-Helmholtz Instability (KHI). We present an overview of 19 MMS observations of the KHI from September 2015 to June 2017. Unitless growth rates and unstable solid angles for each of the 19 events were calculated using 5 techniques to automatically detect plasma regions on either side of the magnetopause boundary. There was no apparent correlation between solar wind conditions during the KHI and its growth rate and unstable solid angle, though we note no KHI were observed for solar wind flow speeds less than 300 km/s or greater than 600 km/s, likely due to a filtering effect of the instability onset criteria and plasma compressibility. Two-dimensional Magnetohydrodynamic (2D MHD) simulations were compared with two of the observed MMS events. Comparison of the observations with the 2D MHD simulations indicates that velocity dependent methods are the most consistent when calculating growth rate and unstable solid angle, but a combination of the velocity dependent and independent methods can be used to select KHI events in which the vortex has rolled over. This may prove useful for future work studying secondary processes associated with the KHI.

1 Introduction

The coupling of the solar wind (SW) to Earth’s magnetosphere and its impacts on local space weather are a fundamental question of space physics. Several mechanisms operating at the magnetopause boundary, such as magnetic reconnection [*Paschmann et al., 1979; Sonnerup et al.; Gosling et al., 1986; Burch and Phan, 2016*] and viscous interactions [*Axford and Hines, 1961; Otto and Fairfield, 2000; Fairfield et al., 2000*], are responsible for the transfer of mass and energy from the solar wind to the magnetosphere. Understanding the detailed effects of these processes is vital to predict and help prevent negative outcomes from space weather.

Observations from Defense Meteorological Satellite Program (DMSP) and Time History of Events and Macroscale Interactions during Substorm (THEMIS) spacecraft have established that the cold component ions of the plasma sheet are 30-40% hotter in the dawn flank than in the dusk [*Hasegawa et al., 2003; Wing et al., 2005; Dimmock et al., 2015*]. *Dimmock et al. [2015]* conducted a statistical study of the magnetosheath source population as observed by THEMIS spacecraft over seven years, which showed ions in

45 the dawn flank are on average 10% hotter than those in the dusk flank. This asymme-
 46 try is more pronounced under fast (> 400 km/s) SW conditions [*Dimmock et al.*, 2015].
 47 However, even during fast SW, the asymmetry of the magnetosheath source plasma is
 48 insufficient to produce the observed asymmetry in the plasma sheet. MHD simulations
 49 were unable to reproduce the observed sheath asymmetry, but it was apparent in hybrid
 50 models, suggesting a kinetic scale mechanism is responsible for asymmetrically driving
 51 the heating of cold component ions in the sheath and further into the magnetosphere [*Dim-*
 52 *mock et al.*, 2015].

53 Several physical mechanisms have been proposed as drivers of the observed plasma
 54 sheet asymmetry. Kelvin-Helmholtz instabilities (KHI), which occur regularly at the mag-
 55 netopause boundary, are one such mechanism [*Otto and Fairfield*, 2000; *Fairfield et al.*,
 56 2000; *Nykyri et al.*, 2003; *Hasegawa et al.*, 2004; *Nykyri et al.*, 2006; *Taylor et al.*, 2008;
 57 *Foullon et al.*, 2008; *Merkin et al.*, 2013; *Lin et al.*, 2014; *Ma et al.*, 2014a,b; *Nykyri et al.*,
 58 2017; *Ma et al.*, 2017; *Sorathia et al.*, 2019]. KHI occur in regions of large shear flow [*Chan-*
 59 *drasekhar*, 1961], such as the boundary between magnetosheath plasma flowing with the
 60 shocked SW and the relatively stagnant magnetosphere [*Miura and Pritchett*, 1982]. Long
 61 established as a source for momentum and energy transport from the SW to the mag-
 62 netosphere [*Miura*, 1984, 1987], later simulations and observations have shown non-linear
 63 stages of the KHI are also capable of reconnection [*Nykyri and Otto*, 2001, 2004; *Nykyri*
 64 *et al.*, 2006; *Hasegawa et al.*, 2009] and ion heating via kinetic wave modes within the
 65 vortices [*Moore et al.*, 2016, 2017]. Compressional waves, like the Kelvin-Helmholtz or
 66 ultra-low frequency (ULF) waves, can also lead to kinetic Alfvén wave (KAW) genera-
 67 tion via mode conversion [*Johson et al.*, 2001; *Chaston et al.*, 2007]. Recent work has sug-
 68 gested that KAWs associated with the KHI can contribute to parallel electron heating,
 69 but are insufficient to account for the total heating [*Nykyri et al.*, 2020]. A detailed mech-
 70 anism for the KHI to develop electron scale waves and quantifying their contribution to
 71 electron heating is still an open question.

72 Observations have shown the the KHI may form on both the dawn and dusk flanks
 73 under any orientation of the interplanetary magnetic field (IMF) [*Kavosi and Reader*,
 74 2015], but simulations have shown a preference for dawn flank formation when the IMF
 75 is in a Parker Spiral (PS) orientation [*Nykyri*, 2013; *Adamson et al.*, 2016]. Recent work
 76 by *Henry et al.* [2017] analyzed the events presented in *Kavosi and Reader* [2015] and
 77 confirmed this preference observationally. *Henry et al.* [2017] also confirmed a preference

78 for KHI formation at the dusk flank for high solar wind speeds under northward IMF
 79 (NIMF). As PS is the most statistically common IMF orientation, it follows that the as-
 80 sociated preference for dawn-side KHI development would also be statistically more com-
 81 mon. Such asymmetry in the formation of KHI, combined with KH-driven secondary pro-
 82 cesses like reconnection and kinetic scale waves, make the KHI a strong candidate to drive
 83 the dawn-dusk asymmetry of cold-component ions in the plasma sheet.

84 The launch of the Magnetospheric Multiscale (MMS) satellites presents a new op-
 85 portunity to extend this study of the KHI and its associated secondary processes to smaller
 86 scales with higher resolution measurements. Within months of its launch, MMS had en-
 87 countered KHI [*Eriksson et al.*, 2016]. The event reported by *Eriksson et al.* [2016] has
 88 been the subject of several case studies: *Li et al.* [2016] found evidence of Alfvénic ion
 89 jets and electron mixing due to reconnection at the trailing edge of the vortex; *Wilder*
 90 *et al.* [2016] noted compressed current sheets and evidence of ion-acoustic waves, and *Stawarz*
 91 *et al.* [2016] took advantage of MMS’s high temporal and spatial resolutions to study tur-
 92 bulence generated by the KHI. These secondary processes would contribute to ion heat-
 93 ing and plasma transfer across the magnetopause boundary.

94 In order to better understand the role KHI and its secondary process play in driv-
 95 ing the plasma sheet asymmetry it is imperative, as a first step, to build a database of
 96 MMS encounters with KHI. The location, duration, and prevailing IMF conditions of each
 97 event are correlated with the unitless growth rates to establish patterns which may prove
 98 informative in understanding the role KHI plays in magnetospheric dynamics (e.g., in
 99 generating dawn-dusk asymmetries via secondary, “cross-scale” processes or affecting the
 100 radiation belt electron populations via ULF wave generation or magnetopause shadow-
 101 ing).

102 In this paper we present a list of MMS encounters with KHI and the physical char-
 103 acteristics of each. The MMS instrumentation and observational signatures used to iden-
 104 tify the KHI encounters are described in Sections 2.2-2.3. Section 2.4 details the method-
 105 ology used to separate magnetosheath and magnetospheric regions of the observed events,
 106 typical parameters of which were used in calculation of the unitless growth rate and un-
 107 stable solid angle for each event. These methodologies were also tested using 2-dimensional
 108 magnetohydrodynamic simulations as described in Section 3. Results and conclusions
 109 are presented and discussed in Section 4.

2 Methodology

2.1 MMS Instrumentation

Observational data reported here is level 2 data from MMS 1 [Burch *et al.*, 2016]. Spacecraft separations are at most 230 km, and more typically on the order of 20 km, well below the typical size of the KHI, thus all spacecraft are expected to observe the same signatures and a single craft is sufficient to identify the KHI. Ion energy spectra and moments are taken from the Fast Plasma Investigation (FPI) [Pollock *et al.*]. The Flux Gate Magnetometers (FGM) were used for the DC magnetic field [Russell *et al.*; Torbet *et al.*, 2016]. Data file versions used are v3.3.0.cdf for FPI and v4.18.0.cdf for FGM. Solar wind data are taken from the OMNI database [King and Papitashvili, 2005].

2.2 Observational Signatures of the KHI

KHI are known to occur at regions of large velocity shear, such as at the flank magnetopause. In this region the magnetosphere is relatively stagnant and plasma in the sheath is accelerating from low speeds immediately after the shock to “catch up” with the solar wind speed downtail [Dimmock and Nykyri, 2013]. At this boundary MMS observes a rapid change in ion bulk velocity on the order of several 100’s of km/s. This change in bulk velocity, however, is characteristic of most boundary crossings even if the boundary is stable. An unstable boundary, which MMS may cross several times, exhibits quasi-periodic fluctuations in ion energies between typical magnetosheath and magnetospheric values. Similarly, anti-correlated quasi-periodic signatures are also observed in the ion temperature and density for an unstable boundary. To distinguish the KHI from a shifting boundary (as a response to SW dynamic pressure variations) or other boundary instabilities (such as flux transfer events (FTE)), MMS is expected to observe quasi-periodic magnetic field fluctuations, particularly in the component of the field normal to the boundary, which indicate twisting of the field lines within the KH vortex. Total field strength will also vary due to compressions by the KHI. The vortex nature of the KHI also creates a force imbalance as the rotational motion creates outward force. This is balanced by a pressure gradient such that a decrease of total pressure is observed at the center of the vortex. Potential KHI events thus show a lower total pressure near the center of the vortex (where \mathbf{B}_N is zero) and higher pressure in the spine region, whereas FTEs

140 are typically associated with an increase in total pressure when \mathbf{B}_N is zero [Nykyri *et al.*,
141 2006; Zhao *et al.*, 2016].

142 Table 1 summarized the 19 MMS encounters of the KHI. Events are evenly distributed
143 between the dawn (9) and dusk (10) flanks. Only two events occur well into the tail, the
144 other 17 are observed sunward of the terminator. This is primarily due to a sampling
145 effect of the MMS phase 1 orbit which targeted dayside magnetopause. Encountered events
146 ranged in duration from as little as 15 minutes to over 2 hours. Examples of two of the
147 listed events (marked with asterisks) are shown in Figures 1 and 2.

152 Table 2 details the prevailing SW conditions for each event. At the time of event
153 onset, IMF configurations are well distributed between Parker spiral (4), northward (3),
154 southward (3), radial (4), dawnward (2), and duskward (3) orientations. However, for
155 the duration of each event, average IMF configurations show a slight preference for the
156 Parker spiral orientation (6), followed by radial and duskward (4 each), northward and
157 southward (2 each), and dawnward (1). None of the the observed events occurred un-
158 der ortho-Parker Spiral IMF orientation. Solar wind flow speeds are never less than 300
159 km/s or greater than 600 km/s. Pressure is typically between 1.4 and 3.5 nPa, with only
160 one event occurring outside this range, with solar wind pressure 5 nPa. Solar wind pa-
161 rameters are discussed in more detail and correlated with the KHI growth rate in Sec-
162 tion 4.

165 Figure 1 shows MMS1 observations of ions from 06:00 to 07:00 on 15 October 2015.
166 MMS passed through the dusk side of the dayside magnetopause during strongly dawn-
167 ward IMF. The omni-directional ion energy spectrogram in panel (a) shows the expected
168 quasi-periodic variations throughout the interval. The magnetic field in panel (b) shows
169 fluctuations characteristic of the KHI from 06:20 to 06:40 and again near 06:50. A ve-
170 locity shear on the order of 200 km/s is visible near 06:25 in panel (c) and anti-correlated
171 fluctuations of ion density and temperature, shown in panel (d), occur throughout the
172 interval. Decreases in total pressure, shown in black in panel (e), are visible starting around
173 06:20.

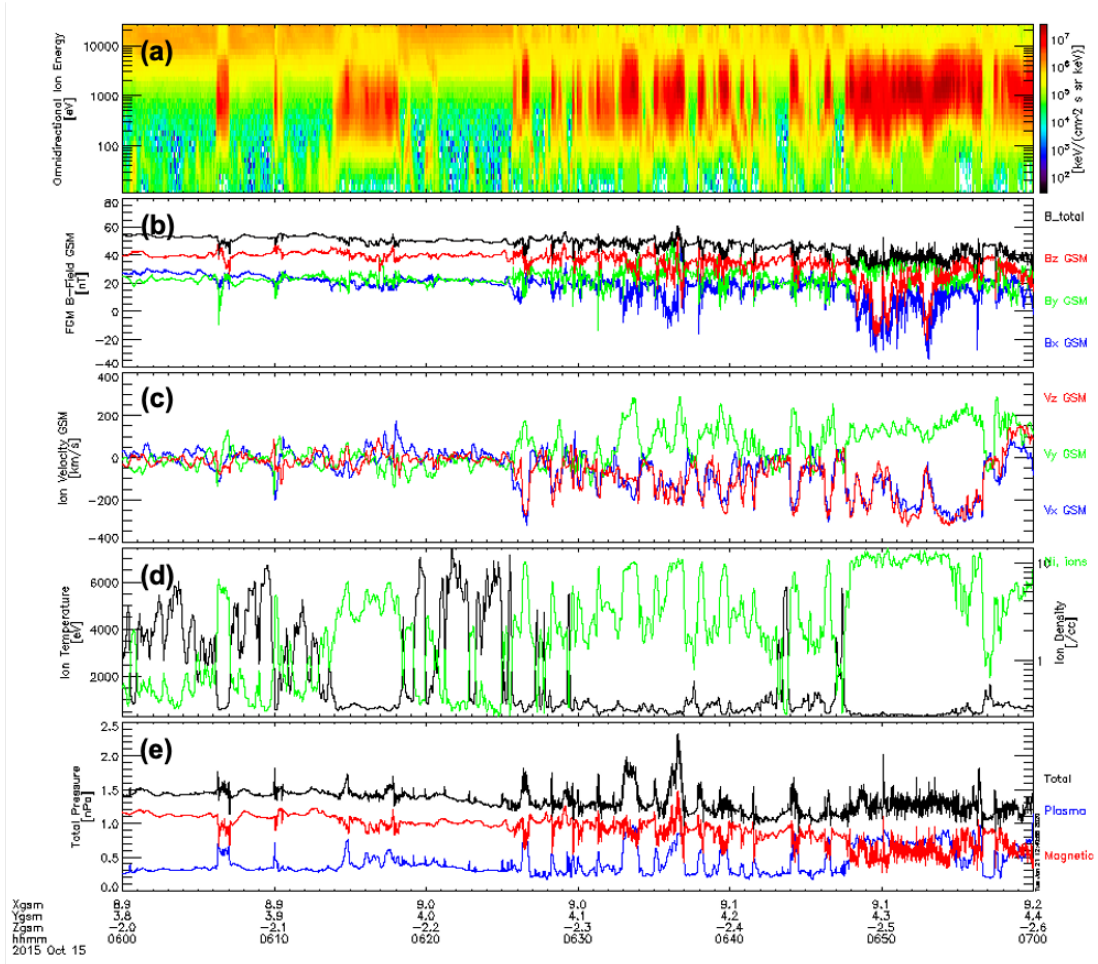
179 MMS observations of another KHI encounter on 26 September 2016 are shown in
180 Figure 2 for the 70 minutes from 14:15 to 15:25. MMS crossed the dusk flank magne-
181 topause while the IMF was in a Parker Spiral orientation. Quasi-periodic fluctuations
182 in omni directional ion spectra are observable from approximately 14:20 to 15:15 in panel

148 **Table 1.** MMS observed 19 KHI from September 2015 to June 2017. The duration and GSM
 149 location of each event are listed. Events were observed equally on the dawn and dusk flanks. The
 150 shortest encounter lasted only 10 minutes, and the longest were 130 minutes. Observations for
 151 marked (*) events are shown in Figures 1 and 2

Date	Onset Time (UT)	Duration (min)	GSM Location (R.E)		
			X	Y	Z
08 Sep 2015	09:20	130	5.0	7.8	-4.5
11 Oct 2015	10:35	20	8.7	6.5	-4.7
*15 Oct 2015	06:05	45	9.0	4.1	-2.3
17 Oct 2015	16:05	22	6.4	7.8	-4.1
18 Oct 2015	15:05	15	7.2	7.5	-4.4
22 Dec 2015	22:20	25	7.9	-5.7	-1.8
11 Jan 2016	20:56	10	6.2	-7.6	-3.4
22 Jan 2016	19:40	40	5.0	-8.5	-5.2
05 Feb 2016	19:00	25	3.3	-9.3	-5.0
07 Feb 2016	03:55	35	7.0	-6.9	-3.5
18 Feb 2016	19:30	55	2.5	-9.7	-6.3
25 Feb 2016	18:55	70	1.3	-9.9	-6.5
*26 Sep 2016	14:30	45	2.7	8.5	-5.4
04 Oct 2016	18:40	40	1.8	11.2	-3.6
10 Oct 2016	14:50	40	4.3	9.3	-5.0
24 Oct 2016	10:55	20	6.8	6.1	-4.3
04 Nov 2016	12:00	50	8.1	7.2	-3.8
03 May 2017	02:10	130	-12.9	-19.7	-3.9
11 May 2017	12:45	70	-15.6	-18.3	1.3

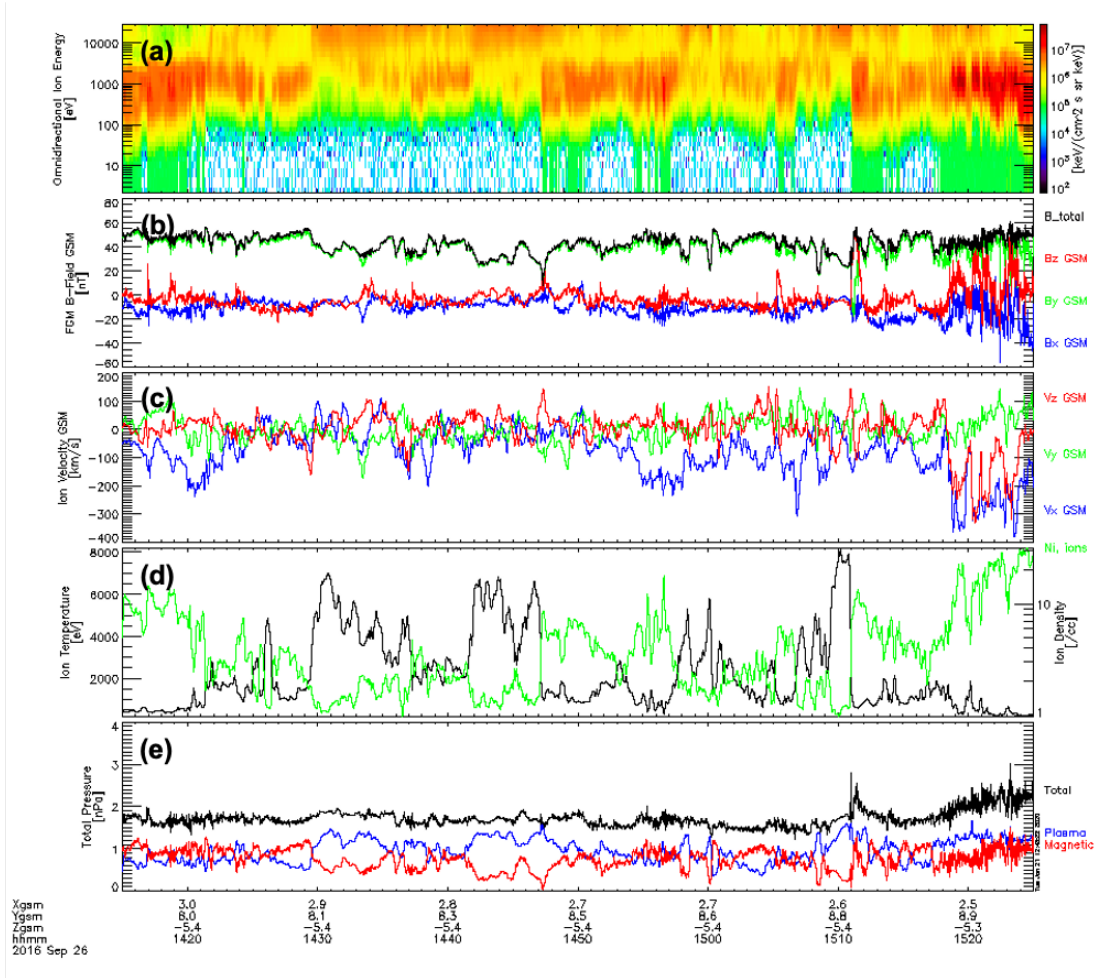
163 **Table 2.** MMS observed 19 KHI from September 2015 to June 2017. Onset and average IMF
 164 orientations and solar wind Alfvén Mach number are determined using OMNI data.

Date	Onset IMF Angles (deg)		Average IMF Angles (deg)		Flow	Alfvén	Pressure
	Clock	Cone	Clock	Cone	Speed (km/s)	Mach Number	(nPa)
08 Sep 2015	12.6	50.6	22.0	52.3	509.2	3.8	5.2
11 Oct 2015	-56.4	123.5	-48.4	111.7	478.0	10.9	1.4
15 Oct 2015	-82.9	92.5	-67.5	94.7	482.7	7.4	1.6
17 Oct 2015	82.2	128.6	-88.8	126.5	345.6	11.5	3.5
18 Oct 2015	-178.6	128.0	-51.1	146.3	454.6	10.5	2.0
22 Dec 2015	-96.9	65.3	129.6	35.8	411.4	7.6	2.0
11 Jan 2016	-113.4	77.8	-116.7	87.8	583.4	4.6	1.7
22 Jan 2016	26.7	15.7	0.5	6.0	493.4	6.3	1.5
05 Feb 2016	-25.7	125.6	-50.5	121.9	470.4	9.4	1.7
07 Feb 2016	42.7	83.4	36.0	78.0	405.3	11.1	2.4
18 Feb 2016	104.3	24.5	-175.1	48.0	594.9	10.2	2.0
25 Feb 2016	-145.6	146.4	-135.0	147.6	302.9	6.5	3.2
26 Sep 2016	-66.0	130.3	-54.6	107.4	430.8	6.8	3.2
04 Oct 2016	-30.0	145.4	86.8	151.7	532.6	9.6	3.2
10 Oct 2016	-86.0	112.5	-62.3	107.7	355.0	9.0	3.0
24 Oct 2016	-15.1	85.4	-21.4	88.7	383.5	9.8	3.5
04 Nov 2016	23.1	120.7	58.8	121.8	370.2	7.6	1.4
03 May 2017	51.4	137.6	49.6	139.7	414.1	14.8	1.4
11 May 2017	60.0	88.6	56.7	81.7	361.4	6.8	2.5



174 **Figure 1.** MMS observations of (a) omnidirectional ion energies; (b) magnetic field in GSM
 175 coordinates; (c) ion bulk velocity in GSM coordinates; (d) ion temperature and density; and (e)
 176 total, magnetic and plasma pressures from 06:00 to 07:00 UT on 15 October 2015. Ion data is
 177 taken from the Fast Plasma Investigation (FPI) and magnetic field data is from the Flux Gate
 178 Magnetometer (FGM) aboard MMS1.

183 (a) and are accompanied by anti-correlated variations in ion density and temperature
 184 (d). Velocity shears (c) on the order of 150-200 km/s occur several times from 14:20 to
 185 15:20. Panel (b) shows fluctuations around 20 nT and up to 40 nT in the magnetic field.
 186 Decreases in total pressure are small, but observable in panel (e) from 14:35 to 15:10.



187 **Figure 2.** MMS observations as in Figure 1 from 14:15 to 15:25 UT on 26 September 2016.
 188 Ion data is taken from the Fast Plasma Investigation (FPI) and magnetic field data is from the
 189 Flux Gate Magnetometer (FGM) aboard MMS1.

190 2.3 Boundary Normal Coordinate System

191 It is useful to rotate observed data into boundary normal (LMN) coordinates for
 192 further analysis. We make use of the maximum variance of the $\mathbf{v} \times \mathbf{B}$ electric field (MVAE)
 193 technique to determine the average outward pointing normal direction, \mathbf{N} for the full du-
 194 ration of each event. The general method for variance analysis techniques is given in *Son-*
 195 *nerup and Scheible* [1998]. *Nykyri et al.* [2011a,b] showed the single spacecraft MVAE
 196 technique is sufficient for identification of the boundary normal direction when the plasma
 197 bulk velocity and magnetic field are primarily tangential to the boundary, as is typically
 198 in the case during KHI. It is also used here, rather than a multi-spacecraft method, to

199 allow for automation of the analysis. For MVAE, the direction in which the electric field
 200 variance is maximized (i.e., the direction of the maximum eigenvector of the MVAE ma-
 201 trix) is taken as the normal direction. Tangential directions are defined by the interme-
 202 diate and minimum eigenvectors of the MVAE matrix, but are not included here. We
 203 use the eigenvalues associated with the maximum and intermediate eigenvectors to de-
 204 termine if the normal direction is well-determined. For a large maximum to intermedi-
 205 ate eigenvalue ratio, $\lambda_{max}/\lambda_{int} > 5$, the normal is clearly determined. Smaller ratios
 206 indicate more ambiguity in the normal direction.

207 In Table 3 the average normal direction and eigenvalue ratio for each event are pre-
 208 sented. Roughly half (9) of the events have a clear, well determined normal direction.
 209 Another two events have only moderately well determined normals ($\lambda_{max}/\lambda_{int} = 4.9$).
 210 The remaining 8 events are ambiguous in their normal direction. Events marked with
 211 an asterisk are examples shown in Figures 3 and 4

216 MVAE analysis also assists in determining how non-linear the KHI may be. Lo-
 217 cal normal directions, \mathbf{n} are calculated every 15 seconds for 1-minute sliding windows for
 218 the duration of each event. The dot product, $\mathbf{n} \cdot \mathbf{N}$, is used to compare the average and
 219 local normal directions. For parallel \mathbf{n} and \mathbf{N} , $\mathbf{n} \cdot \mathbf{N} = 1$, and there is no twisting of
 220 the boundary layer. As the boundary layer is twisted in the non-linear KHI $\mathbf{n} \cdot \mathbf{N} \rightarrow$
 221 -1 . The local normal is not required to be outward pointing, but the shift from an out-
 222 ward to inward pointing normal is expected to be gradual [Nykyri *et al.*, 2006]. Sudden
 223 shifts are most likely due to the 180 degree ambiguity in the MVAE technique.

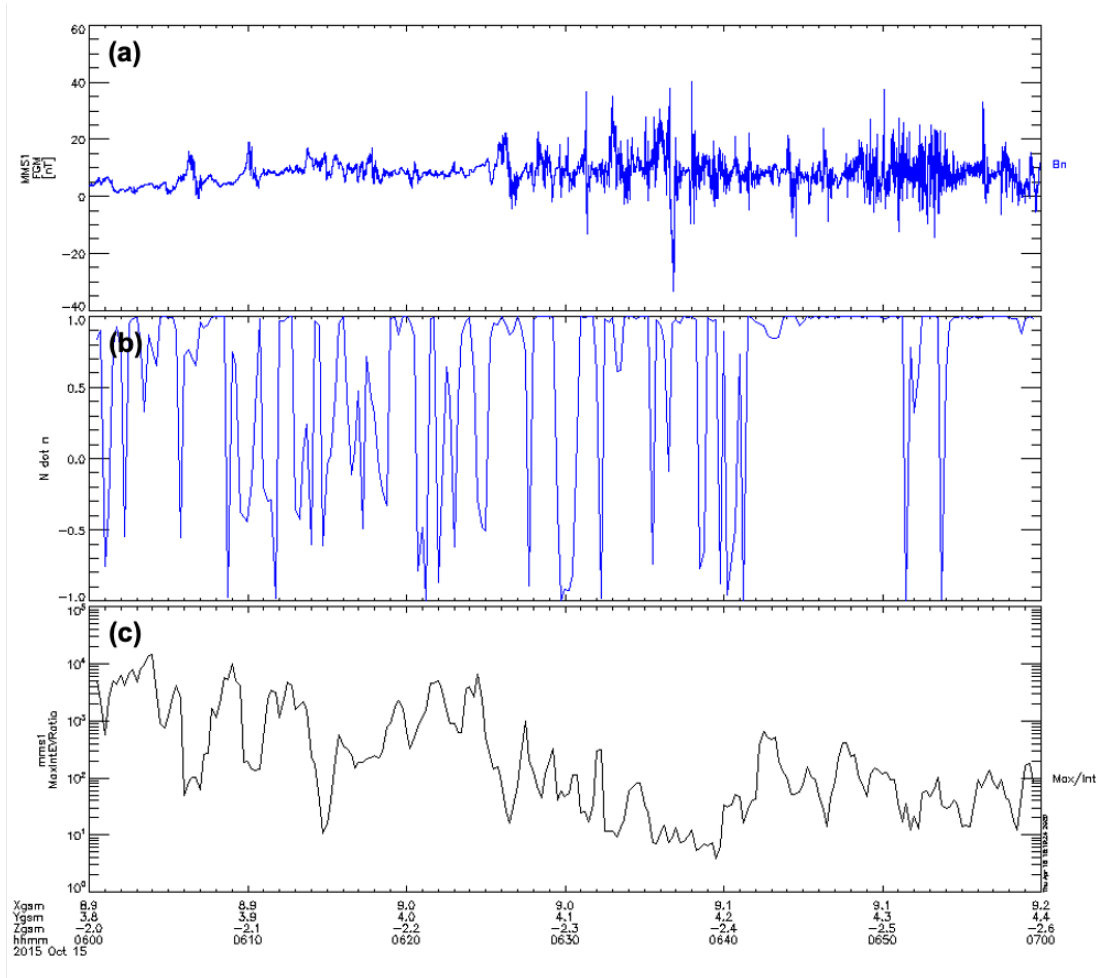
224 The 15th October 2015 event is shown in boundary normal coordinates from 06:00
 225 to 07:00 in Figure 3. After rotating to the LMN system, the normal component of the
 226 magnetic field showed strong fluctuations, on the order of 20-40 nT (a). For this event
 227 the normal direction was was (0.779,0.266,-0.568) in GSM, which was well determined
 228 with an eigenvalue ratio of 10.401. Figure 3 shows evidence of boundary twisting from
 229 06:00 to 06:40 (b). The boundary normal direction for each window was well determined,
 230 as shown by large value of the maximum to intermediate eigenvalue ratio (c). Because
 231 the average and local normal directions are all well-determined throughout the interval,
 232 this event is probably in a non-linear stage of development.

233 Figure 4 shows the KHI encounter from 14:15 to 15:25 on 26 September 2016 in
 234 boundary normal coordinates. Fluctuations of 20-40 nT in the normal magnetic field com-

212 **Table 3.** The outward pointing normal to the boundary layer is identified as the direction of
 213 maximum variance in the $\mathbf{v} \times \mathbf{B}$ electric field. This direction is well determined when the max-
 214 imum eigenvalue significantly larger than the intermediate eigenvalue, yielding an eigenvalue
 215 ratios of 5 or greater.

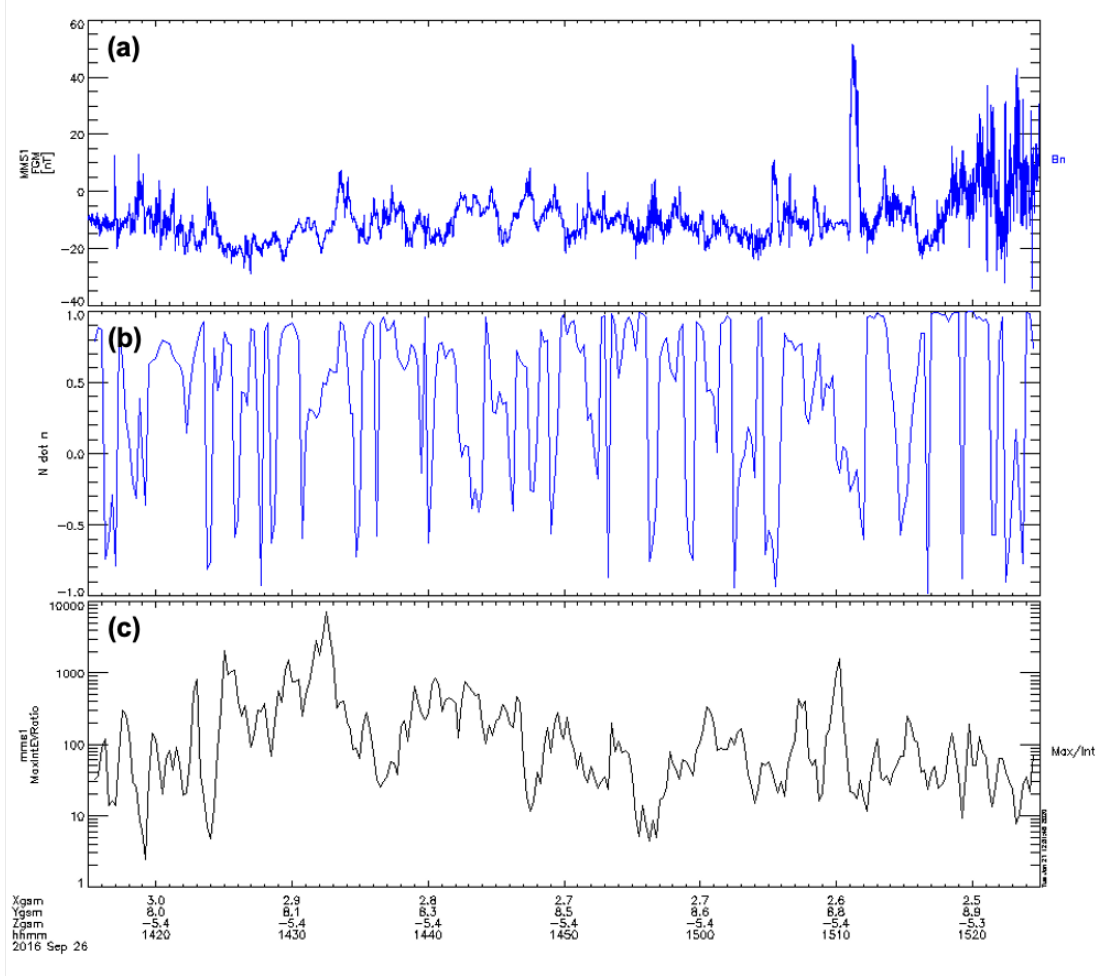
Date	GSM Location (R.E)			Boundary Normal Direction			Average
	X	Y	Z	X	Y	Z	Eigenvalue Ratio
08 Sep 2015	5.0	7.8	-4.5	0.67	0.56	0.50	19.3
11 Oct 2015	8.7	6.5	-4.7	0.81	0.35	-0.47	8.8
15 Oct 2015	9.0	4.1	-2.3	0.78	0.27	-0.57	10.4
17 Oct 2015	6.4	7.8	-4.1	0.80	0.44	-0.40	3.9
18 Oct 2015	7.2	7.5	-4.4	0.80	0.35	-0.49	13.7
22 Dec 2015	7.9	-5.7	-1.8	0.78	-0.34	-0.53	4.9
11 Jan 2016	6.2	-7.6	-3.4	0.65	-0.40	-0.65	7.5
22 Jan 2016	5.0	-8.5	-5.2	0.56	-0.40	-0.72	1.6
05 Feb 2016	3.3	-9.3	-5.0	0.50	-0.50	-0.71	1.5
07 Feb 2016	7.0	-6.9	-3.5	0.86	-0.34	-0.39	3.8
18 Feb 2016	2.5	-9.7	-6.3	0.42	-0.39	-0.82	3.0
25 Feb 2016	1.3	-9.9	-6.5	0.54	-0.63	-0.56	14.4
26 Sep 2016	2.7	8.5	-5.4	0.48	0.32	-0.81	2.0
04 Oct 2016	1.8	11.2	-3.6	0.52	0.64	-0.57	2.6
10 Oct 2016	4.3	9.3	-5.0	0.72	0.48	-0.50	4.9
24 Oct 2016	6.8	6.1	-4.3	0.80	0.33	-0.49	13.5
04 Nov 2016	8.1	7.2	-3.8	0.78	0.38	-0.49	2.9
03 May 2017	-12.9	-19.7	-3.9	0.22	-0.95	-0.23	5.1
11 May 2017	-15.6	-18.3	1.4	0.18	-0.97	0.14	9.6

235 ponent are clear throughout the interval (a). The average normal direction for this event
 236 is (0.484,0.323,-0.813) in GSM. Given a 1.993 eigenvalue ratio, the average normal di-
 237 rection is not clearly determined. Panel (b) of Figure 4 shows twisting of the local bound-
 238 ary away from the average normal at semi-regular intervals for the the duration of the
 239 event. Local normals are generally well determined, as shown by eigenvalue ratios con-
 240 sistently on the oder of 10-100 (c).



241 **Figure 3.** The (a) normal component of the magnetic field, (b) dot product of local and
 242 average normal directions, and (c) ratio of maximum and intermediate eigenvalues for each local
 243 window are derived from MMS1 FGM and FPI observations from 06:00 to 07:00 on 15 October
 244 2015.

247 Having identified MMS encounters with the KHI, we next calculate the growth rates
 248 of the events and compare them with the prevailing solar wind and IMF properties.



245 **Figure 4.** Quantities, as in Figure 3, are derived from MMS1 FGM and FPI observations
 246 from 14:15 to 15:25 on 126 September 2016.

249 2.4 Calculation of the Instability Growth Rate

250 Any region unstable to the KHI will satisfy the KHI instability criteria

$$[\mathbf{k} \cdot (\mathbf{v}_1 - \mathbf{v}_2)]^2 \geq \frac{n_1 + n_2}{4\pi m_0 n_1 n_2} [(\mathbf{k} \cdot \mathbf{B}_1)^2 + (\mathbf{k} \cdot \mathbf{B}_2)^2] \quad (1)$$

251 where \mathbf{v}_i , n_i , and \mathbf{B}_i are the the velocity, density, and magnetic field on either side of
 252 the velocity shear layer and \mathbf{k} is the wave vector [Chandrasekhar, 1961]. Note this equa-
 253 tion is merely an approximation of the instability for an observed event as it assumes
 254 an infinitely thin boundary layer which is not true for the magnetopause. Equation 1 also
 255 assumes an incompressible plasma, yet for high (> 600 km/s) solar wind speeds, the com-
 256 pressibility is sufficient to stabilize the development of the KHI. Furthermore, MMS will
 257 not necessarily observe the source region of the KHI and local conditions may not match

258 those of the source region. Equation 1 may be rearranged to determine the normalized
 259 growth rate of the KHI in a particular region, which is defined as

$$Q/k = \sqrt{a_1 a_2 (\Delta \mathbf{v} \cdot \hat{\mathbf{k}})^2 - a_1 (\mathbf{v}_{A1} \cdot \hat{\mathbf{k}})^2 - a_2 (\mathbf{v}_{A2} \cdot \hat{\mathbf{k}})^2} \quad (2)$$

where a_i is a density parameter for either side of the boundary defined by $a_i = \rho_i / (\rho_1 + \rho_2)$, \mathbf{v}_{Ai} is the Alfvén velocity on either side, and $\hat{\mathbf{k}}$ is the unit wave vector (thus the growth rate is normalized to the wavelength), pointing in the direction of maximum growth. In order to compare the normalized growth rates for KHI events observed at various locations and under a variety of SW and IMF conditions, we make it completely unitless via comparison with the local fast mode speed, $v_{fm} = \sqrt{v_A^2 + c_s^2}$. The fast mode speed is not equal in the magnetosheath (sub-index *msh*) and magnetosphere (sub-index *msh*) regions, so we normalize to the mean of the two, such that

$$Q_{unitless} = \frac{Q/k}{v_{fm}}$$

260 where $v_{fm} = \frac{1}{2}(v_{fmmsh} + v_{fmmsh})$.

261 In Equation 2 the direction of $\hat{\mathbf{k}}$ is chosen to maximize the normalized growth rate,
 262 but many directions of $\hat{\mathbf{k}}$ may satisfy the instability criteria. This range of angles capa-
 263 ble of satisfying the instability criteria can be used to determine just how susceptible a
 264 region is to the development of KHI.

265 KHI may propagate in any direction $\hat{\mathbf{k}}$ for which Q/k is positive. If we express $\hat{\mathbf{k}}$
 266 in terms of the spherical angles ϕ and θ , the percent of the 4π solid angle that satisfies
 267 the KHI instability criteria at a given location may be calculated. We use the term this
 268 percentage the “unstable solid angle.” Events with larger growth rates and/or larger un-
 269 stable solid angles are likely to be KHI.

270 Calculation of the unitless growth rate and unstable solid angle requires the iden-
 271 tification of separate regions of magnetosheath and magnetospheric plasma on either side
 272 of the magnetopause boundary. The unperturbed flank magnetosheath is characterized
 273 by cold, dense plasma flowing tailward at high speeds with the shocked SW. In contrast
 274 the magnetospheric plasma is hot, tenuous, and relatively stagnant. Using several com-
 275 binations of density, temperature, and the X -component of the bulk velocity we devel-
 276 oped five methods to separate data from the magnetosheath and magnetosphere regions,
 277 allowing automated growth rate calculations. The isolated data was then used to deter-

278 mine characteristic values of each region for calculation of the growth rate and unsta-
 279 ble solid angle.

280 **2.4.1 Density-Temperature Ratio Methods**

281 Method 1 uses a ratio of the ion density and average temperature, n/T , to iden-
 282 tify the separate regions. The largest 20% and smallest 20% of all n/T values in the ob-
 283 servation interval are used to calculate a typical value of n/T value at the magnetopause
 284 boundary, n/T_{mp} , for each interval. In the cold and dense magnetosheath n/T is signif-
 285 icantly greater than in the hot and tenuous magnetosphere, so regions with $n/T > 1.5n/T_{mp}$
 286 or $n/T < .5n/T_{mp}$ are classified as the magnetosheath or magnetospheric regions, re-
 287 spectively. We avoid any ambiguous and mixed regions, thus only the plasma param-
 288 eters of pristine magnetosheath and magnetosphere are used in calculation of the growth
 289 rate and unstable solid angle. The regions identified using this method are marked in
 290 yellow (magnetosheath) and blue (magnetosphere) in Figure 5 for the 15 October 2015
 291 event and Figure 6 for the event on 26 September 2016.

292 Method 1 is appropriate for linear stages of the KHI, but may fail for non-linear
 293 stages. In cases of rolled-up, non-linear KHI, a portion of the magnetospheric plasma
 294 may be accelerated within the vortex and carried tailward with the magnetosheath. Ac-
 295 celeration within the late stage KHI cannot have a physical effect on the development
 296 and initial growth rate, but without constraining the velocity this accelerated plasma
 297 may be identified with the magnetosphere and affect the initial conditions used in cal-
 298 culations. To avoid this issue, the mean and standard deviation of the tailward (X -component)
 299 magnetosheath velocity are found, and the magnetospheric region is constrained to plasma
 300 with tailward flow at least one standard deviation slower than the mean sheath speed,
 301 such that $v_{Xmsp} < v_{Xmsh} - \sigma_{v_{Xmsh}}$. Portions of the previously identified magnetosphere
 302 that fulfill the criteria are marked in green in Figure 5 and 6 for the example events.

310 As can be seen in Figures 5 and 6 both Methods 1 and 2 identify only a small por-
 311 tion of the intervals as magnetosheath. MMS data does suggest the spacecraft spent less
 312 time in the sheath than in the magnetosphere, but the omnidirectional energy spectro-
 313 gram (panels (c) in Figures 5 and 6) show several regions (6:20 to 6:41 in 5, 14:56 and
 314 15:11 in 6) which appear to have sheath like populations that these methods classified
 315 as ambiguous and/or mixed. A much larger region is identified as the magnetosphere and

316 is only slightly reduced when we constrain the velocity signature of the region. This indi-
 317 cates the velocity constraint is useful in accounting for the effects of rolled-up of the
 318 vortex.

319 In both methods, mean values for velocity, magnetic field, and density in either re-
 320 gion are used to calculate the unitless growth rate and unstable solid angle. Results of
 321 these calculations for all the of identified MMS KHI encounters may be found in Table
 322 5 and Table 6.

323 ***2.4.2 Specific Entropy Methods***

324 Method 3 uses the specific entropy, $S = T/n^{2/3}$, rather than n/T , to identify the
 325 regions on either side of the boundary layer. Again the largest and smallest 20% of all
 326 S values in an interval are used to determine the typical value at the magnetopause bound-
 327 ary, S_{mp} , for each event. The specific entropy of the magnetosheath is expected to be
 328 significantly less than the magnetosphere, so regions with $S < 0.5S_{mp}$ are sorted to the
 329 magnetosheath and regions with $S > 1.5S_{mp}$ are sorted to the magnetosphere. In this
 330 method, as with the density-temperature ratio methods, ambiguous and mixed regions
 331 are avoided when calculating characteristic parameters for each region. The sheath, as
 332 identified using the specific entropy, is marked in yellow in Figure 7 and 8 for the 15 Oc-
 333 tober 2015 and 26 September 2016 events respectively; the magnetosphere is marked in
 334 blue.

335 As in the density-temperature ratio, identification of the sheath and magnetosphere
 336 using specific entropy does not consider the expected velocity differences in the regions,
 337 thus it may be less effective for rolled-up KHI vortices. Again we require the magneto-
 338 spheric plasma be flowing tailward at least one standard deviation slower than the sheath
 339 ($v_{Xmsp} < v_{Xmsh} - \sigma_{v_{Xmsh}}$). The remaining magnetospheric regions meeting this con-
 340 straint are marked in green in Figure 7 and 8.

348 Using this methodology, a much larger portion of each event is classified as mag-
 349 netosheath plasma, including some intervals that appear mixed and ambiguous in the
 350 MMS data (6:30 to 6:43, 6:44 to 6:47 in Figure 7 and 14:47 to 14:58, 15:11 to 15:17 in
 351 Figure 8). The magnetosphere accounts for only a few minutes of the example events,
 352 in direct contradiction to the regions identified using the density-temperature ratio. Con-
 353 straining the velocity required in the magnetosphere, reduces the region even further,

354 to the point MMS does not spend enough time in the region to calculate reliable plasma
 355 parameters.

356 Results for the growth rate and unstable solid angles using mean sheath and mag-
 357 netosphere parameters as determined with both the unconstrained and velocity-constrained
 358 specific entropy methods are reported in Table 5 and Table 6.

359 *2.4.3 Density and Velocity Method*

360 The final method uses the product of density and tailward (GSE/GSM X -component)
 361 velocity, nv_x to separate regions of the sheath and magnetospheric plasma. As in all other
 362 methods, the mean of the largest and smallest 20% of nv_x values in the interval are used
 363 as the typical magnetopause value, nv_{Xmp} . In the shocked SW of the magnetosheath,
 364 nv_x is large and negative, while it is small in the stagnant magnetosphere. Thus the mag-
 365 netosheath comprises regions of $nv_x < nv_{Xmp}$, and the magnetosphere comprises re-
 366 gions of $nv_x > nv_{Xmp}$. Mixed and ambiguous regions are not avoided in this method,
 367 thus the presence of a significant transition layer will affect the normalized growth rate.
 368 The sheath and magnetosphere identified using this method are marked in yellow and
 369 blue respectively for the 15 October 2015 event in Figure 9 and for the 26 September 2016
 370 event in Figure 10.

377 Unlike the previous methods, mixed and ambiguous regions are intentionally in-
 378 cluded in this method. This avoids the exclusion of relevant intervals, but can also un-
 379 predictably affect the parameters used for the growth rate calculation. In both exam-
 380 ple cases only a small portion of the interval is classified as the magnetosheath and sev-
 381 eral regions, which exhibit sheath like characteristics, are instead sorted into the mag-
 382 netosphere (6:06, 6:14 to 6:19 in Figure 9 and 14:48 to 14:52 in Figure 10).

383 Values of the unitless growth rate and unstable solid angle of all the events found
 384 using the density-velocity product are reported in Table 5 and Table 6.

385 Unitless growth rate is not a perfect parameter to describe the KHI. The KHI is
 386 a convective instability which dissipates stored energy as it develops, thus growth rate
 387 and the unstable solid angle are maximized just prior to the formation of the KHI. The
 388 nature of in-situ observations, however, dictates we cannot identify KHI until they are
 389 relatively well developed. Thus small growth rates and unstable solid angles are not nec-

390 necessarily counter-indicative of KHI, but may instead be features of later stage KHI. As
 391 KHI develop, they may form non-linear vortices, which can be seen in observations as
 392 low density magnetospheric plasma flowing tailward with the magnetosheath [*Hasegawa*
 393 *et al.*, 2006; *Taylor et al.*, 2012]. Figure 11 plots tailward velocity as a function of ion
 394 density for the event on (top) 15 October 2015 and (bottom) 26 September 2016. Color
 395 overlays correspond with (left) the density temperature ratio, n/T ; (center) specific en-
 396 tropy, S ; and (right) the density-tailward velocity product nv_X . Red to orange points
 397 are magnetospheric values, blue to green are the sheath. As expected from Figures 5 and
 398 6, the n/T parameter identifies only a few points in the sheath, and indicates a signif-
 399 icant amount of the magnetospheric plasma moving tailward with the magnetosheath,
 400 as in a rolled up vortex. The specific entropy method, on the other hand indicates no
 401 magnetospheric plasma flows with the magnetosheath, but also indicates almost no mag-
 402 netospheric plasma generally. The method using the product of the density and tailward
 403 velocity yields the largest mixed region of any of the methods, with only a small por-
 404 tion of the data identified as the magnetosheath. Any indication of a non-linear rolled-
 405 up vortex is obscured by the large number of mixed and ambiguous data points.

411 3 Comparison with Simulations

412 To verify our method for the calculation of normalized growth rates is robust it was
 413 applied to parameters generated by two dimensional MHD simulations of KHI. A sim-
 414 ulation case for the KHI developing under Northward IMF (NIMF) conditions was tested
 415 using initial conditions comparable to those of the event on 08 September 2015. A sec-
 416 ond simulation case used initial conditions similar to those of the 18 October 2015 event
 417 for the KHI developing on the dusk flank under Parker Spiral IMF (PSIMF).

418 The simulations, after *Ma et al.* [2019], solve the full set of resistive Hall-MHD equa-
 419 tions equations using a leapfrog scheme [*Potter*, 1973; *Birn*, 1980; *Otto*, 1990]. We nor-
 420 malize all physical quantities to their typical scale, for example, the length L is normal-
 421 ized to L_0 , the half width of the initial sheered flow; number density to n_0 , the magnetic
 422 field to B_0 , velocity to the Alfvén velocity, $V_A = B/\sqrt{\mu_0\rho_0}$; and the time to the Alfvén
 423 transit time. The values of the these normalizations for each simulation case are sum-
 424 marized in Table 4

425

Table 4. Normalization constants for the 2D MHD simulations.

Quantity	Northward	Parker spiral
Magnetic field B_0 (nT)	71.5	33.38
Number Density n_0 (/cc)	12.36	6.45
Length scale L_0 (km)	640	640
Velocity V_A (km/s)	443	286.5
Time t_0 (s)	1.35	2.23

426

427

428

429

430

431

432

433

434

A cut was taken through the KHI vortex in the simulation box every 10 time steps. Data from these cuts was separated into distinct regions using the methods described in Sections 2.4.1 - 2.4.3 and used to calculate growth rates and unstable solid angles. The growth rates as a function of time are shown on the left of Figures 12 and 13 for the PSIMF and NIMF cases respectively; examples of the density within the KHI and the cuts used for calculations (red) are shown on the right. The "true" growth rate, as determined by the linear slope of a plot of $\ln(v_{\perp})$ as a function of time, is also shown (solid black line). In both cases, all methods overestimate the growth rate, which is expected as the calculation assumes an infinitely thin boundary layer and incompressible plasma.

442

443

444

445

446

447

448

449

As can be seen in Figures 12 and 13 for the PSIMF and NIMF cases, respectively, all methods produced very similar results until vortex roll-over was captured by the cut. After roll-over occurred, the velocity-independent methods saw a sharp decrease in growth rate. The velocity dependent methods remained roughly consistent throughout roll-over and saw a more gradual decrease in growth rate as the instability dissipated. We do note that the method using a product of density and tailward velocity behaved more unpredictably than the other velocity dependent methods. This is likely due to the inclusion of mixed and ambiguous regions with this method.

450

451

452

453

454

The unstable solid angle followed a similar pattern as the unitless growth rate, but remained near its minimum value longer than the growth rate. Both simulation cases produced a larger initial growth rates and unstable solid angles than the observational events they were based on. As the the simulations progressed however, the growth rate and unstable solid angle decreased to roughly match the observational case, and at later

455 simulation times, some methods produced unstable solid angles less than the MMS ob-
 456 servations.

457 **4 Conclusions and Discussion**

458 The main conclusions may be summarized as follows:

- 459 • MMS observed 19 clear KHI events from September 2015 to June 2017.

460 From September 2015 to June 2017 MMS observed more than 80 mixed regions which
 461 initially resembled KHI. Further analysis of growth rate calculations, total pressure and
 462 boundary-normal rotated magnetic field showed 19 of these events likely to be KHI. These
 463 19 events, summarized in Table 1, were evenly distributed between the dawn and dusk
 464 flanks and occur under a variety of prevailing SW conditions and IMF orientations.

- 465 • A method combining the density-temperature ratio and tailward velocity of a KHI
 466 event is most consistent at automatically identifying regions of magnetosheath and
 467 magnetospheric plasma for calculation of the KHI growth rate and unstable solid
 468 angle.

469 Five methods are developed to separate the sheath and magnetospheric regions in
 470 the MMS data. Mean parameters from each region are used to calculate the unitless growth
 471 rate and unstable solid angle for each of the 19 events. Results of the growth rate and
 472 unstable solid angle calculations for all methods are presented in Table 5 and Table 6
 473 respectively. When the results of the calculations are considered with the identified re-
 474 gions, mean parameters of each region, and the results of the simulations, we find the
 475 velocity constrained density-temperature ratio method is the most robust and reliable
 476 in separating the sheath and magnetosphere plasmas.

477 The density-temperature ratio methods have a tendency to neglect some appar-
 478 ently sheath-like regions, and thus tailward velocity in the sheath is somewhat overes-
 479 timated. This overestimation is consistent and predictable. Constraining the velocity sig-
 480 nificantly increases the growth rate in some, but not all cases, suggesting this is a use-
 481 ful method for identifying and characterizing rolled up, non-linear KHI vortices.

482 The entropy methods are the least reliable. Identified sheath regions include many
 483 intervals that do not exhibit sheath-like characteristics despite having low entropy.

484 Thus the sheath velocity and density are much lower than expected. The reduced ve-
 485 locity shear and density parameters result in low growth rates. Constraining the tail-
 486 ward velocity universally increases the growth rate due to the severely reduced magne-
 487 tospheric region (see green boxes in Figures 8 and 7), such that the sample size is too
 488 small to produce reliable parameters for the growth rate calculation. This may be an ef-
 489 fect of the conservation of specific entropy across the boundary.

490 Use of the product of density and tailward velocity has inconsistent effects on the
 491 growth rate. Including mixed and ambiguous regions avoids the exclusion of relevant in-
 492 tervals seen in the other methods, but can also unpredictably affect the parameters used
 493 for the growth rate calculation. This is particularly pronounced in the simulation cases,
 494 where the identified values of physical parameters (density, temperature, etc.) for each
 495 distinct region approached the same value as the simulation progressed. This method
 496 appears less reliable than the velocity constrained density-temperature ratio when con-
 497 sidering rolled-up KHI vortices.

- 498 • A comparison of two methods, the density-temperature ratio with and without
 499 constraints on the tailward velocity, is an effective way to identify KHI vortices which
 500 have rolled-over.

501 Constraining the magnetospheric velocity for both the density-temperature ratio
 502 and entropy methods increased the final growth rate. In several cases this increase was
 503 an insignificant fraction of the growth rate, which we believe indicates MMS encountered
 504 a more linear stage of the KHI where very little if any magnetospheric plasma had been
 505 rolled-up in the vortex and accelerated downtail with the sheath. More significant in-
 506 creases in growth rate indicate a larger fraction of the previously identified magnetosphere
 507 was moving with the sheath, as expected for a non-linear rolled-up KH vortex. For only
 508 one event under either methodology (24 Oct 2016 for density-temperature ratio and 18
 509 Feb 2016 for entropy) did the unitless growth rate decrease when velocity was constrained.

510 Unstable solid angles follow the same patterns as the unitless growth rate. When
 511 comparing the velocity constrained and unconstrained methods those events with insignif-
 512 icant increases in unstable solid angle match exactly the events with insignificant increases
 513 in growth rate. The same is true for cases with large increases and cases with decreases.

514 This further suggests the comparison of the methods with and without constraints on
 515 velocity are able consistently able to indicate if a KHI vortex has rolled over.

- 516 • The KHI is observed only when solar wind flow speeds are between 300 and 600
 517 km/s. KHI growth rates are otherwise independent of the prevailing solar wind
 518 conditions.

519 Values of the unitless growth rate for each event using all 5 methods described in
 520 Sections 2.4.1 - 2.4.3 are presented in Table 5. Figure 14 then plots the mean unitless
 521 growth rates of all events as a function of (a) solar wind density, (b) temperature, (c)
 522 flow speed, (d) pressure, (e) IMF magnitude, and (f) Alfvén Mach number. Growth rates
 523 appear to be independent of most solar wind parameters, with the exception of solar wind
 524 flow speed. All of the observed events occurred when the solar wind was between 300
 525 and 600 km/s. At flow speeds below 300 km/s the velocity shear is too low to satisfy the
 526 KHI onset conditions. At solar wind speeds above 600 km/s the compressibility of the
 527 plasma can stabilize the KHI [*Miura and Pritchett, 1982*]. Within this selection window,
 528 flow speed and growth rate are not correlated.

- 536 • The KHI is observed only when solar wind flow speeds are between 300 and 600
 537 km/s. Unstable solid angles are otherwise independent of the prevailing solar wind
 538 conditions.

539 Table 6 lists the unstable solid angle of each KHI event calculated using the 5 meth-
 540 ods described in Sections 2.4.1 - 2.4.3. The mean unstable solid angles for all events are
 541 plotted as function of (a) solar wind density, (b) temperature, (c) flow speed, (d) pres-
 542 sure, (e) IMF magnitude, and (f) Alfvén Mach number in Figure 15. As with the growth
 543 rates, unstable solid angles show no apparent correlation with solar wind conditions, with
 544 the exception of a selection window from 300 to 600 km/s flow speed. This confirms that
 545 KHI develop within an ideal plasma velocity range, such that the velocity is high enough
 546 (> 300 km/s) to satisfy the onset criteria, but not so high (> 600 km/s) as to produce
 547 high compressibility for typical magnetosheath plasma.

556 We note several of the observed events occur in apparently stable regions with very
 557 low growth rates; this does not preclude the observed events from being KHI. Convec-
 558 tive instabilities like KHI dissipate energy stored in unstable regions and systems. As

529 **Table 5.** Unitless growth rates describe the speed at which the KHI develops as a fraction
 530 of the local mean fast mode speed for each of the 19 MMS encounters. Parameters for each re-
 531 gion both the sheath and magnetospheric regions were identified using 5 methods described in
 532 Sections 2.4.1 - 2.4.3.

Event Date	n/T	$n/T, v_x$	S	S, v_x	nv_x	MEAN
08 Sep 2015	0.129	0.130	0.059	0.059	0.133	0.102
11 Oct 2015	0.018	0.018	0.031	0.032	0.004	0.021
15 Oct 2015	0.009	0.008	0.010	0.011	0.085	0.024
17 Oct 2015	0.027	0.037	0.014	0.018	0.068	0.033
18 Oct 2015	0.064	0.060	0.063	0.063	0.099	0.070
22 Dec 2015	0.001	0.020	0.002	0.005	0.044	0.014
11 Jan 2016	0.026	0.052	0.011	0.034	0.017	0.028
22 Jan 2016	0.014	0.012	0.004	0.009	0.029	0.014
05 Feb 2016	0.046	0.049	0.002	0.007	0.045	0.030
07 Feb 2016	0.004	0.019	0.010	0.019	0.012	0.013
18 Feb 2016	0.043	0.059	0.008	0.006	0.060	0.035
25 Feb 2016	0.021	0.045	0.008	0.039	0.023	0.027
26 Sep 2016	0.100	0.106	0.027	0.037	0.123	0.079
04 Oct 2016	0.043	0.080	0.005	0.041	0.078	0.049
10 Oct 2016	0.079	0.084	0.026	0.043	0.090	0.064
24 Oct 2016	0.013	0.007	0.001	0.001	0.011	0.007
04 Nov 2016	0.028	0.035	0.016	0.021	0.036	0.027
03 May 2017	0.155	0.169	0.165	0.171	0.134	0.159
11 May 2017	0.127	0.130	0.021	0.055	0.134	0.093

548 **Table 6.** The unstable solid angle is the percent of the total 4π solid angle which is unstable
 549 to the development of the KHI. For each of the 19 MMS KHI encounters parameters for the
 550 two sheath and magnetospheric regions are identified using each of the 5 methods described in
 551 Sections 2.4.1 - 2.4.3.

Event Date	n/T	$n/T, v_x$	S	S, v_x	nv_x	MEAN
08 Sep 2015	6.93	6.98	3.83	3.84	6.97	5.71
11 Oct 2015	0.26	0.31	2.10	2.21	0.04	0.98
15 Oct 2015	0.07	0.06	0.25	0.30	5.48	1.23
17 Oct 2015	1.28	2.32	0.44	0.58	4.77	1.88
18 Oct 2015	5.68	6.12	5.39	5.39	7.62	6.04
22 Dec 2015	0.00	0.56	0.01	0.03	1.95	0.51
11 Jan 2016	0.73	2.65	0.15	1.27	0.22	1.00
22 Jan 2016	0.21	0.11	0.02	0.05	0.92	0.26
05 Feb 2016	5.21	5.56	0.02	0.14	3.66	2.92
07 Feb 2016	0.01	0.16	0.21	0.46	0.06	0.18
18 Feb 2016	5.24	7.72	0.11	0.07	5.88	3.80
25 Feb 2016	0.23	1.38	0.04	0.92	0.30	0.57
26 Sep 2016	7.47	8.22	2.35	3.37	9.64	6.21
04 Oct 2016	3.04	7.16	0.10	4.07	7.62	4.40
10 Oct 2016	7.14	7.73	2.44	4.19	7.56	5.81
24 Oct 2016	0.10	0.06	0.00	0.00	0.11	0.05
04 Nov 2016	1.35	1.83	0.80	1.08	1.93	1.40
03 May 2017	19.14	21.40	18.44	19.14	14.50	18.52
11 May 2017	12.14	12.53	0.65	6.24	12.54	8.82

559 excess energy is dissipated, the region becomes more stable, thus maximum instability
 560 and growth rates occur just prior to the formation of the instability. KHI, by necessity,
 561 are only observed after instability and growth rates have decreased from their maxima.
 562 We believe those events occurring in apparently more stable regions are simply later in
 563 development than faster growing KHI in less stable areas.

564 **Acknowledgments**

565 Funding for this work was provided by the National Science Foundation under grant num-
 566 ber 1707521 and by NASA under grants numbers NNZ17AI50G and NNX16AF89G. Thanks
 567 are owed to the entire MMS team, and especially to the FGM and FPI instrument groups.
 568 MMS data was retrieved from the MMS Science Data Center at [lasp.Colorado.edu/mms/sdc/public](http://lasp.colorado.edu/mms/sdc/public).
 569 OMNI solar wind data is available from NASA Goddard Space Flight Center’s Space Physics
 570 Data Facility at omniweb.gsfc.nasa.gov.

571 **References**

- 572 Adamson, E., K. Nykyri, and A. Otto (2016), The Kelvin-Helmholtz Instability un-
 573 der Parker-Spiral Interplanetary Magnetic Field Conditions at the Magnetospheric
 574 Flanks, *Advances in Space Research*, *58*.
- 575 Axford, W., and C. Hines (1961), A Unifying Theory of High-Latitude Phenomena
 576 and Geomagnetic Storms, *Canadian Journal of Physics*, *39*, 1433–1464.
- 577 Birn, J. (1980), Computer Studies of the Dynamic Evolution of the Geomagnetic
 578 Tail, *Journ. of Geophys. Res.*, *85*, 1214–1222.
- 579 Burch, J. L., and T. D. Phan (2016), Magnetic Reconnection and the Dayside
 580 Magnetopause: Advances with MMS, *Geophys. Res. Lett.*, *43*, 8327–8338, doi:
 581 10.1002/2016GL069787.
- 582 Burch, J. L., T. E. Moore, R. B. Torbet, and B. L. Giles (2016), Magnetospheric
 583 Multiscale Overview and Science Objectives, *Space Science Reviews*, *199*, 5–21,
 584 doi:10.1007/s11214-015-0164-9.
- 585 Chandrasekhar, S. (1961), *Hydrodynamic and Hydromagnetic Stability*, Oxford Uni-
 586 versity Press.
- 587 Chaston, C. C., M. Wilber, M. Fujimoto, M. L. Goldstein, M. Acuna, H. Rme,
 588 and A. Fazakerley (2007), Mode Conversion of Anomalous Transport in Kelvin-
 589 Helmholtz Vortices and Kinetic Alfvén Waves at Earth’s Magnetopause, *Physical*

590 *Review Letters*, 99.

- 591 Dimmock, A. P., and K. Nykyri (2013), The Statistical Mapping of Magnetosheath
 592 Plasma Properties Based on THEMIS Measurements in the Magnetosheath Inter-
 593 planetary Medium Reference Frame, *Journ. of Geophys. Res.*, 118, 4963–4876.
- 594 Dimmock, A. P., K. Nykyri, H. Karimbadi, A. Osmane, and T. I. Pulkkinen (2015),
 595 A statistical study into the spatial distribution and dawn-dusk asymmetry of
 596 dayside magnetosheath ion temperatures as a function of upstream solar wind
 597 conditions, *Journ. of Geophys. Res.*, 120, 2767–2782, doi:10.1002/2014JA020734.
- 598 Eriksson, S., B. Lavraud, F. D. Wilder, J. E. Stawarz, B. L. Giles, J. L. Burch,
 599 W. Baumjohann, R. E. Ergun, P.-A. Lindqvist, W. Magnes, C. J. Pollock, C. R.
 600 Russel, Y. Saito, R. J. Strangeway, R. B. Torbert, D. J. Gershmann, Y. V.
 601 Khotyaintsev, J. C. Dorelli, S. J. Schwartz, L. Avanov, E. Grimes, Y. Vernisses,
 602 A. P. Sturmer, T. D. Phan, G. T. Marklund, T. E. Moore, W. R. Paterson, and
 603 K. A. Goodrich (2016), Magnetospheric Multiscale Observations of Magnetic
 604 Reconnection Associated with Kelvin-Helmholtz Waves, doi:10.
- 605 Fairfield, D. H., A. Otto, T. Mukai, S. Kokubun, R. P. Lepping, J. T. Steinberg,
 606 A. J. Lazaurs, and T. Yamamoto (2000), Geotail observations of the Kelvin-
 607 Helmholtz instability at the equatorial magnetotail boundary for parallel north-
 608 ward fields, *Journ. of Geophys. Res.*
- 609 Foullon, C., C. J. Farrugia, A. N. Fazakerley, C. J. Owen, F. T. Gratton, and R. B.
 610 Torbert (2008), Evolution of Kelvin-Helmholtz Activity on the Dusk Flank Mag-
 611 netopause, *Journ. of Geophys. Res.*, 113, doi:10.1029/2008JA013175.
- 612 Gosling, J. T., M. F. Thomsen, S. J. Bame, and C. T. Russell (1986), Accelerated
 613 Plasma Flows at the Near-Tail Magnetopause, *Journ. of Geophys. Res.: Space*
 614 *Physics*, 91, doi:10.1029/JA091iA03p03029.
- 615 Hasegawa, H., M. Fujimoto, K. Maezawa, Y. Saito, and T. Mukai (2003), Geo-
 616 tail observation of the dayside outer boundary region: Interplanetary magnetic
 617 field control and dawn-dusk asymmetry, *Journ. of Geophys. Res.*, 108, doi:
 618 10.1029/2002JA009667.
- 619 Hasegawa, H., M. Fujimoto, T.-D. Phan, H. Réme, A. Balogh, M. W. Dunlop,
 620 C. Hashimoto, and R. TanDokoro (2004), Transport of solar wind into Earth's
 621 magnetosphere through rolled-up Kelvin-Helmholtz vortices, *Nature*, 430, 755–758.

- 622 Hasegawa, H., M. Fujimoto, K. Takagi, Y. Saito, T. Mukai, and H. Réme (2006),
 623 Single-spacecraft detection of rolled-up Kelvin-Helmholtz vortices at the flank
 624 magnetopause, *Journ. of Geophys. Res.*, *111*, doi:10.1029/2006JA011728.
- 625 Hasegawa, H., A. Reino, A. Vaivads, Y. Khotyaintsev, M. Andre, T. K. M. Naka-
 626 mura, L.-L. Teh, B. U. O. Sonnerup, S. J. Schwartz, Y. Seki, M. Fujimoto,
 627 Y. Saito, H. Reme, and P. Canu (2009), Kelvin-Helmholtz waves at the Earth's
 628 magnetopause: Multiscale development and associated reconnection, *Geophys.*
 629 *Res. Lett.*, *114*, doi:10.1029/2009JA014042.
- 630 Henry, Z. W., K. Nykyri, T. W. Moore, A. P. Dimmock, and X. Ma (2017), On the
 631 Dawn-Dusk Asymmetry of the Kelvin-Helmholtz Instability between 2007 and
 632 2013, *Journ. of Geophys. Res.*, *122*, 11,888–11,900, doi:10.1002/2017JA024548.
- 633 Johson, J. R., C. Z. Cheng, and P. Song (2001), Signatures of Mode Conversion and
 634 Kinetic Alfvén Waves at the Magnetopause, *Geophys. Res. Lett.*, *28*.
- 635 Kavosi, S., and J. Reader (2015), Ubiquity of Kelvin-Helmholtz waves at the Earth's
 636 Magnetopause, *Nature Communications*.
- 637 King, J. H., and N. E. Papitashvili (2005), Solar Wind Spatial Scales in and Com-
 638 parisons of Hourly Wind And ACE Plasma and Magnetic Field Data, *Journ. of*
 639 *Geophys. Res.*, *110*, doi:10.1029/2004JA010649.
- 640 Li, W., M. Andre, Y. V. Khotyaintsev, A. Vaivads, D. B. Graham, S. Toledo-
 641 Redondo, C. Norgren, P. Henri, C. Wang, B. B. Tang, B. Lavraud, Y. Vernisse,
 642 D. L. Turner, J. Burch, R. Torbet, W. Magnes, C. T. Russell, J. B. Blake,
 643 B. Mauk, B. Giles, C. Pollock, J. Fennell, A. Jaynes, L. A. Avanov, J. C. Dorellie,
 644 D. J. Gershman, W. R. Paterson, Y. Saito, and R. J. Strangeway (2016), Kinetic
 645 Evidence of Magnetic Reconnection due to Kelvin-Helmholtz Waves, *Geophys.*
 646 *Res. Lett.*, *43*, 5635–5643, doi:10.1002/2016GL069192.
- 647 Lin, D., C. Wang, W. Li, B. Tang, X. Guo, and Z. Peng (2014), Properties of
 648 Kelvin-Helmholtz Waves at the Magnetopause under Northward Interplanetary
 649 Magnetic Field: Statistical Study, *Journ. of Geophys. Res.: Space Physics*, *119*,
 650 7485–7494, doi:10.1002/2014JA020379.
- 651 Ma, X., A. Otto, and P. Delamere (2014a), Interaction of Magnetic Reconnection and
 652 Kelvin-Helmholtz Modes for Large Magnetic Shear: 1. Kelvin-Helmholtz Trigger,
 653 *Journ. of Geophys. Res.: Space Physics*.

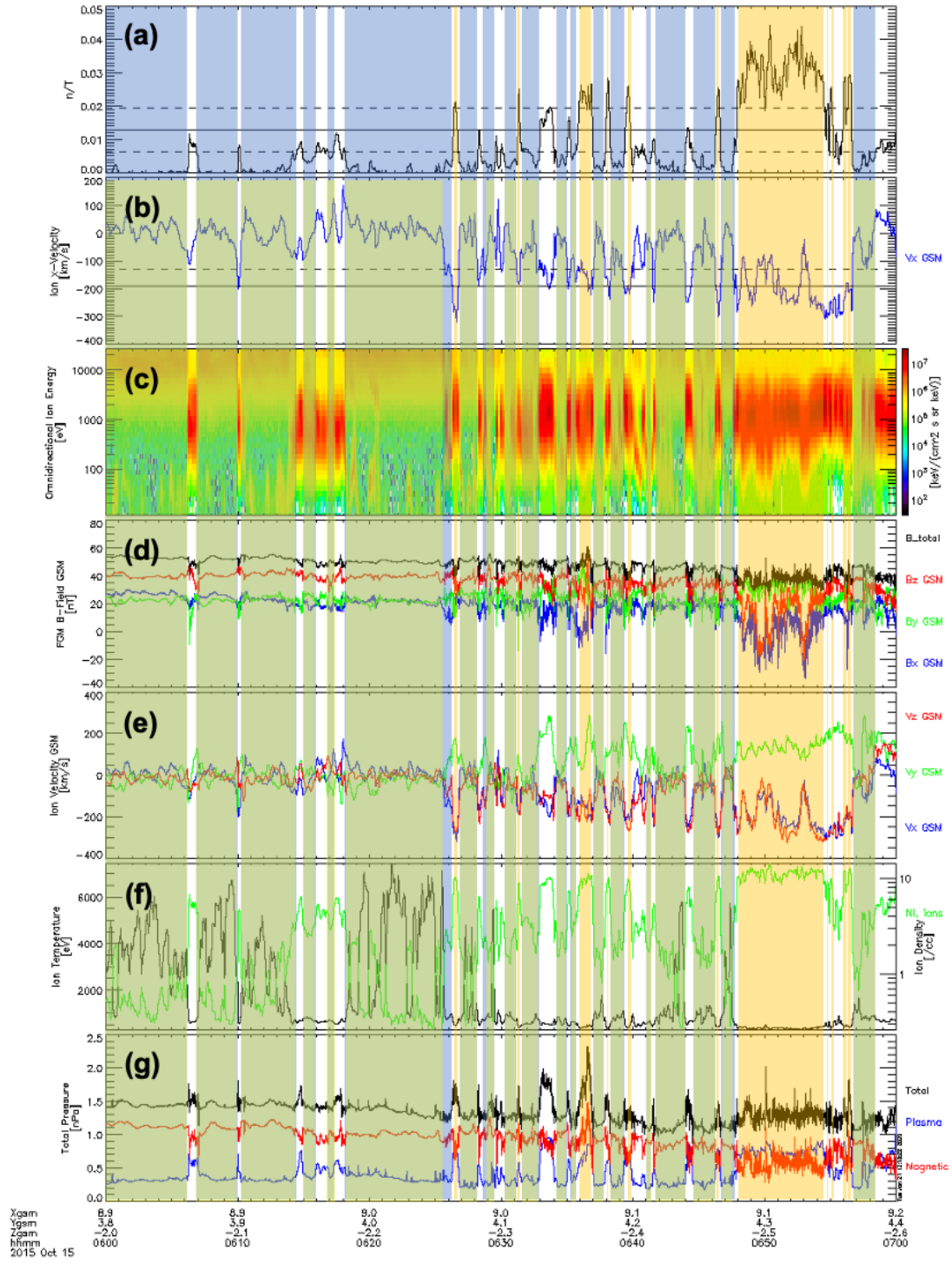
- 654 Ma, X., A. Otto, and P. Delamere (2014b), Interaction of Magnetic Reconnection
 655 and Kelvin-Helmholtz Modes for Large Magnetic Shear: 2. Reconnection Trigger,
 656 *Journ. of Geophys. Res.: Space Physics*.
- 657 Ma, X., P. Delamere, A. Otto, and B. Burkholder (2017), Plasma Transport Driven
 658 by the Three-Dimensional Kelvin-Helmholtz Instability, *Journ. of Geophys. Res.:*
 659 *Space Physics*, 122.
- 660 Ma, X., P. Delamere, K. Nykyri, B. Burkholder, D. Neupane, and R. Rice (2019),
 661 Comparison Between Fluid Simulation With Test Particles and Hybrid Simulation
 662 for the Kelvin-Helmholtz Instability, *Journ. of Geophys. Res.: Space Physics*, 124.
- 663 Merkin, V. G., J. G. Lyon, and S. G. Claudepierre (2013), Kelvin-Helmholtz In-
 664 stability of the Magnetospheric Boundary in a Three-Dimensional Global MHD
 665 Simulation During Northward IMF Conditions, *Journ. of Geophys. Res.: Space*
 666 *Physics*, 118, 5478–5496, doi:10.1002/jgra.50520.
- 667 Miura, A. (1984), Anomalous Transport by Magnetohydrodynamic Kelvin-Helmholtz
 668 Instabilities in the Solar Wind-Magnetosphere Interaction, *Journ. of Geophys.*
 669 *Res.*, 89, 801–818.
- 670 Miura, A. (1987), Simulation of the Kelvin-Helmholtz Instability at the Magneto-
 671 spheric Boundary, *Journ. of Geophys. Res.*, 92, 3195–3206.
- 672 Miura, A., and P. L. Pritchett (1982), Nonlocal Stability of Analysis of the MHD
 673 Kelvin-Helmholtz Instability in a Compressible Plasma, *Journ. of Geophys. Res.*,
 674 87, 7431–7444.
- 675 Moore, T. W., K. Nykyri, and A. P. Dimmock (2016), Cross-scale energy transport
 676 in space plasmas, *Nature Physics*.
- 677 Moore, T. W., K. Nykyri, and A. P. Dimmock (2017), Ion-Scale Wave Properties
 678 and Enhanced Ion Heating Across the Low-Latitude Boundary Layer During
 679 Kelvin-Helmholtz Instability, *Journal of Geophysical Research: Space Physics*, 122,
 680 11,128–11,153, doi:10.1002/2017JA024591.
- 681 Nykyri, K. (2013), Impact of MHD Shock Physics on Magnetosheath Asymmetry
 682 and Kelvin-Helmholtz Instability, *Journal of Geophysical Research: Space Physics*,
 683 118, 5068–5081.
- 684 Nykyri, K., and A. Otto (2001), Plasma transport at the magnetopause boundary
 685 due to reconnection in Kelvin-Helmholtz vortices, *Geophys. Res. Lett.*, 28, 3565–
 686 3568.

- 687 Nykyri, K., and A. Otto (2004), Influence of the Hall term on KH instability and
 688 reconnection inside KH vortices, *Ann. Geophys.*, *22*, 935–949.
- 689 Nykyri, K., A. Otto, J. Büchner, B. Nikutowski, W. Baumjohann, L. M. Kistler,
 690 and C. Mouikis (2003), Equator-S Observations of Boundary Signatures: FTE’s
 691 or Kelvin-Helmholtz Waves?, in *Earth’s Low-Latitude Boundary Layer, Geophys-*
 692 *ical Monograph*, vol. 133, edited by P. T. Newell and R. Onsager, pp. 205–210,
 693 American Geophysical Union.
- 694 Nykyri, K., A. Otto, B. Lavraud, C. Mouikis, L. M. Kistler, A. Balogh, and
 695 H. Réme (2006), Cluster observations of reconnection due to the Kelvin-Helmholtz
 696 instability at the dawnside magnetospheric flank, *Ann. Geophys.*, *24*, 2619–2643.
- 697 Nykyri, K., A. Otto, E. Adamson, and J. Mumme (2011a), Cluster Observations of
 698 a Cusp Diamagnetic Cavity: Structure, Size, and Dynamics, *Journ. of Geophys.*
 699 *Res.*, *116*.
- 700 Nykyri, K., A. Otto, E. Adamson, and A. Tjulin (2011b), On the Origin of Fluc-
 701 tuation in the Cusp Diamagnetic Cavity, *Journ. of Geophys. Res.*, *116*, doi:
 702 10.1029/2010JA015888.
- 703 Nykyri, K., X. Ma, A. Dimmock, C. Foullon, A. Otto, and A. Osmane (2017),
 704 Influence of Velocity Fluctuations on the Kelvin-Helmholtz Instability and
 705 its Associated Mass Transport, *Journ. of Geophys. Res.*, *122*, 9489–9512, doi:
 706 10.1002/2017JA024374.
- 707 Nykyri, K., X. Ma, B. Burkholder, R. Rice, J. Johnson, E.-K. Kim, P. Delamere,
 708 A. Michael, K. Sorathia, D. Lin, S. Merkin, S. Fuselier, J. Broll, O. L. Contel,
 709 D. Gershman, I. Cohen, B. Giles, R. J. Strangeway, C. T. Russell, and J. Burch
 710 (2020), MMS Observations of the Multi-Scale Wave Structures and Parallel Elec-
 711 tron Heating in the Vicinity of the Southern Exterior Cusp, *Journ. of Geophys.*
 712 *Res.: Space Physics*.
- 713 Otto, A. (1990), 3D Resistive MHD Computations of Magnetospheric Physics, *Com-*
 714 *puter Physics Communications*, *59*, 185–195.
- 715 Otto, A., and D. H. Fairfield (2000), Kelvin-Helmholtz Instability at the Magnetotail
 716 Boundary: MHD Simulation and Comparison with Geotail Observations, *Journ.*
 717 *of Geophys. Res.*, *105*, 21,175–21,190.
- 718 Paschmann, G., B. O. . Sonnerup, I. Papamastorakis, G. Haerendel, S. J. Bame,
 719 J. R. Asbridge, J. T. Gosling, C. T. Russell, and R. C. Elphric (1979), Plasma

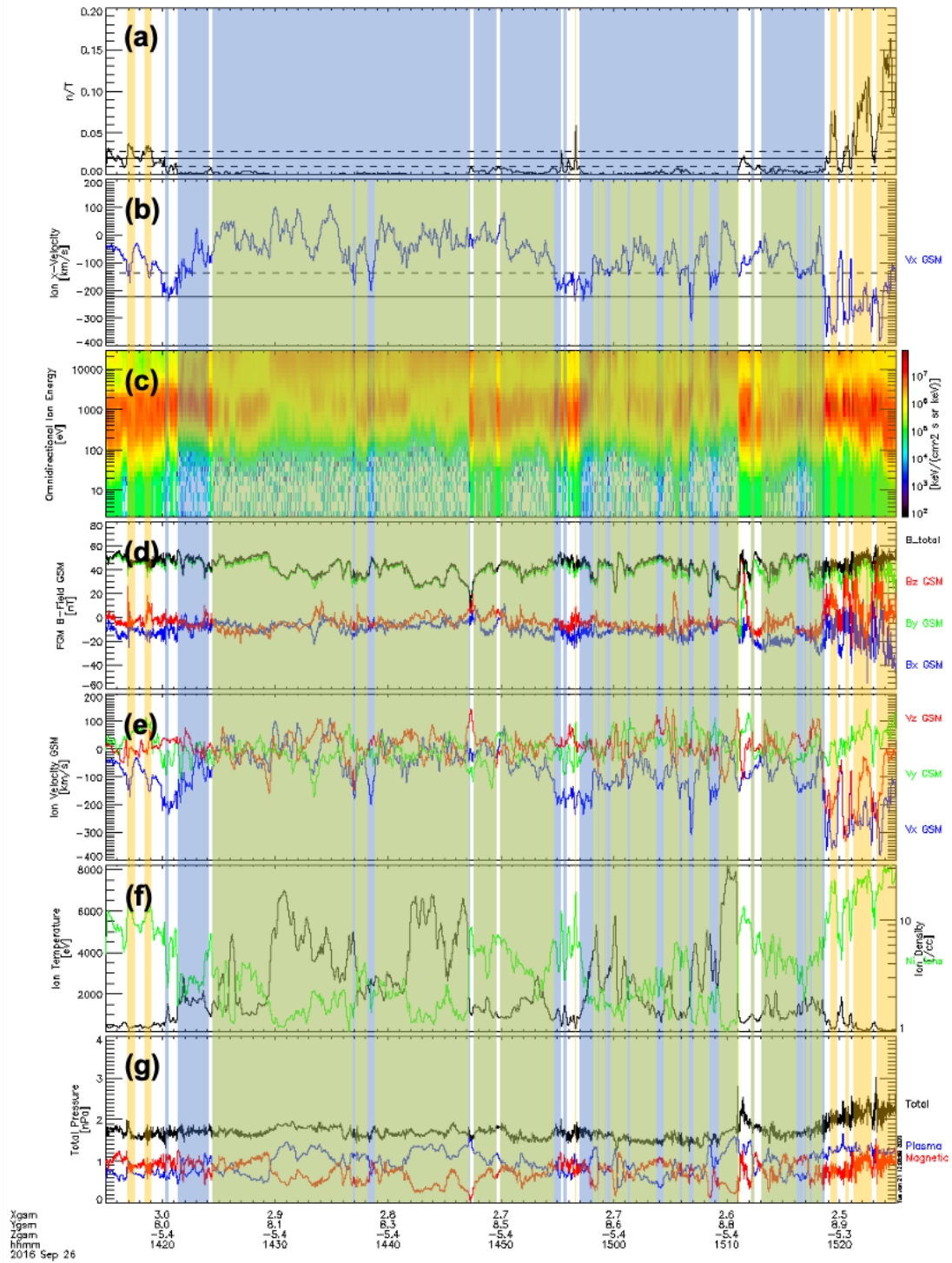
- 720 Acceleration at the Earth's Magnetopause: Evidence for Reconnection, *Nature*,
721 *282*, 243–246.
- 722 Pollock, C., T. Moore, A. Jacques, J. Burch, U. Gliese, Y. Saito, T. Omoto,
723 L. Avanov, A. Barrie, V. Coffey, J. Dorelli, D. Gershman, B. Giles, T. Ros-
724 nack, C. Salo, S. Yokota, M. Adrian, C. Aoustin, C. Auletti, S. Aung, V. Bigio,
725 N. Cao, M. Chandler, D. Chornay, K. Christian, G. Clark, G. Collinson, T. Cor-
726 ris, A. D. L. Santos, R. Devlin, T. Diaz, T. Dickerson, C. Dickson, A. Diekmann,
727 F. Diggs, C. Duncan, A. Figueroa-Vinas, C. Firman, M. Freeman, N. Galassi,
728 K. Garcia, G. Goodhart, D. Guererro, J. Hageman, J. Hanley, E. Hemminger,
729 M. Holland, M. Hutchins, T. James, W. Jones, S. Kreisler, J. Kujawaski, V. Lavu,
730 J. Lobell, E. LeCompte, A. Lukemire, E. MacDonald, A. Mariano, T. Mukai,
731 K. Narayanan, Q. Nguyen, M. Onizuka, W. Paterson, S. Persyn, B. Piepgrass,
732 F. Cheey, A. Rager, T. Raghuram, A. Ramil, L. Reichenthal, H. Rodriguez,
733 J. Rouzaud, A. Rucker, Y. Saito, M. Samara, J.-A. Sauvaud, D. Schuster,
734 M. Shappirio, K. Shelton, D. Sher, D. Smith, K. Smith, S. Smith, D. Steinfeld,
735 R. Szymkiewicz, K. Tanimoto, J. Taylor, C. Tucker, K. Tull, A. Uhl, J. Vloet,
736 P. Walpole, S. Weidner, D. White, G. Winkert, P.-S. Yeh, and M. Zeuch (), Fast
737 Plasma Investigation for Magnetospheric Multiscale, journal =.
- 738 Potter, D. (1973), *Computational Physics*, John Wiley and Sons.
- 739 Russell, C. T., B. J. Anderson, W. Baumjohann, K. R. Bromund, D. Dearborn,
740 D. Fischer, G. Le, H. K. Leinweber, D. Lenema, W. Magnes, J. D. Means, M. B.
741 Moldwin, R. Nakamura, D. Pierce, F. Plaschke, K. M. Rowe, J. A. Slavin, R. J.
742 Strangeway, R. Torbet, C. Hagen, I. Jernej, A. Valavanoglou, and I. Richter ().
- 743 Sonnerup, B. U. O., and M. Scheible (1998), *Minimum and Maximum Variance*
744 *Analysis*, pp. 185–220, International Space Science Institute.
- 745 Sonnerup, B. U. ., G. Paschmann, I. Papamastorakis, N. Sckopke, G. Haerendel,
746 S. J. Bame, J. R. Asbridge, J. T. Gosling, and C. T. Russell (), Evidence for Mag-
747 netic Field Reconnection at the Earth's Magnetopause, *Journ. of Geophys. Res.:*
748 *Space Physics*.
- 749 Sorathia, K. A., V. G. Merkin, A. Y. Ukhorskiy, R. C. Allen, K. Nykyri, and
750 S. Wing (2019), Solar Wind Ion Entry into the Magnetosphere During North-
751 ward IMF, *Journ. of Geophys. Res.: Space Physics*, *124*.

- 752 Stawarz, J. E., S. Eriksson, F. D. Wilder, R. E. Ergun, S. J. Schwartz, A. Pou-
753 quet, J. L. Burch, B. L. Giles, Y. Khotyaintsev, O. L. Contel, P.-A. Lindqvist,
754 W. Magnes, C. J. Pollock, C. T. Russell, R. J. Strangeway, R. B. Torbert, L. A.
755 Avakov, J. C. Dorelli, J. P. Eastwood, D. J. Gershman, K. A. Goodrich, D. M.
756 Malaspina, G. T. Marklund, L. Mirioni, and A. P. Sturmer (2016), Observations
757 of Turbulence in a Kelvin-Helmholtz Event on 8 September 2015 by the Mag-
758 netospheric Multiscale mission, *Journ. of Geophys. Res.*, *121*, 11,021–11,034,
759 doi:10.1002/10JA023458.
- 760 Taylor, M. G. G. T., B. Lavraud, C. P. Escoubet, S. E. Milan, K. Nykyri, M. W.
761 Dunlop, J. A. Davies, R. H. W. Friedel, H. Frey, Y. V. Bogdanova, A. Asnes,
762 H. Laakso, P. Trvincek, A. Masson, H. Opgenoorth, C. Vallat, A. N. Fazaker-
763 ley, A. D. Lahiff, C. J. Owen, F. Pitout, Z. Pu, C. Shen, Q. G. Zong, H. Rme,
764 J. Scudder, and T. L. Zhang (2008), The Plasma Sheet and Boundary Layers un-
765 der Northward IMF: A Multi-point and Multi-instrument Perspective, *Advances*
766 *in Space Research*, *41*, 1619–1629.
- 767 Taylor, M. G. G. T., H. Hasegawa, B. Lavraud, T. Phan, C. P. Escobet, M. W. Dun-
768 lop, Y. V. Bogdanova, A. L. Borg, M. Volwerk, J. Berchem, O. D. Constantinescu,
769 J. P. Eastwood, A. Masson, H. Laakso, J. Soucek, A. N. Fazakerley, H. Frey,
770 E. V. Panov, C. Shen, J. K. Shi, D. G. Sibeck, Z. Y. Pu, J. Wang, and J. A. Wild
771 (2012), Spatial distribution of rolled up Kelvin-Helmholtz vortices at Earth’s
772 dayside and flank magnetopause, *Ann. Geophys.*
- 773 Torbet, R. B., C. T. Russell, W. Magnes, R. E. Ergun, P.-A. Lindqvist, O. LeCon-
774 tel, H. Vaith, J. Macri, S. Myers, D. Rau, J. Needell, B. King, M. Granoff,
775 M. Chutter, I. Dors, G. Olsson, Y. V. Khotyaintsev, A. Eriksson, C. A. Klet-
776 zing, S. Bounds, B. Anderson, W. Baumjohann, M. Steller, K. Bromund,
777 G. Le, R. Nakamura, R. J. Strangeway, H. K. Leinweber, S. Tucker, J. Westfell,
778 D. Fisher, F. Plaschke, J. Porter, and K. Lappalainen (2016), The FIELDS In-
779 strument Suite on MMS: Scientific Objectives, Measurements, and Data Products,
780 *Space Science Reviews*, *199*, 105–135, doi:10.1007/s11214-014-0109-8.
- 781 Wilder, F. D., R. E. Ergun, S. J. Schwartz, D. L. Newman, S. Eriksson, J. E.
782 Stawarz, M. V. Goldman, K. A. Goodrich, D. J. Gershman, D. M. Malaspina,
783 J. C. Holmes, A. P. Sturmer, J. L. Burch, R. B. Torbert, P.-A. Lindqvist, G. T.
784 Marklund, Y. Khotyaintsev, R. J. Strangeway, C. T. Russell, C. J. Pollock, B. L.

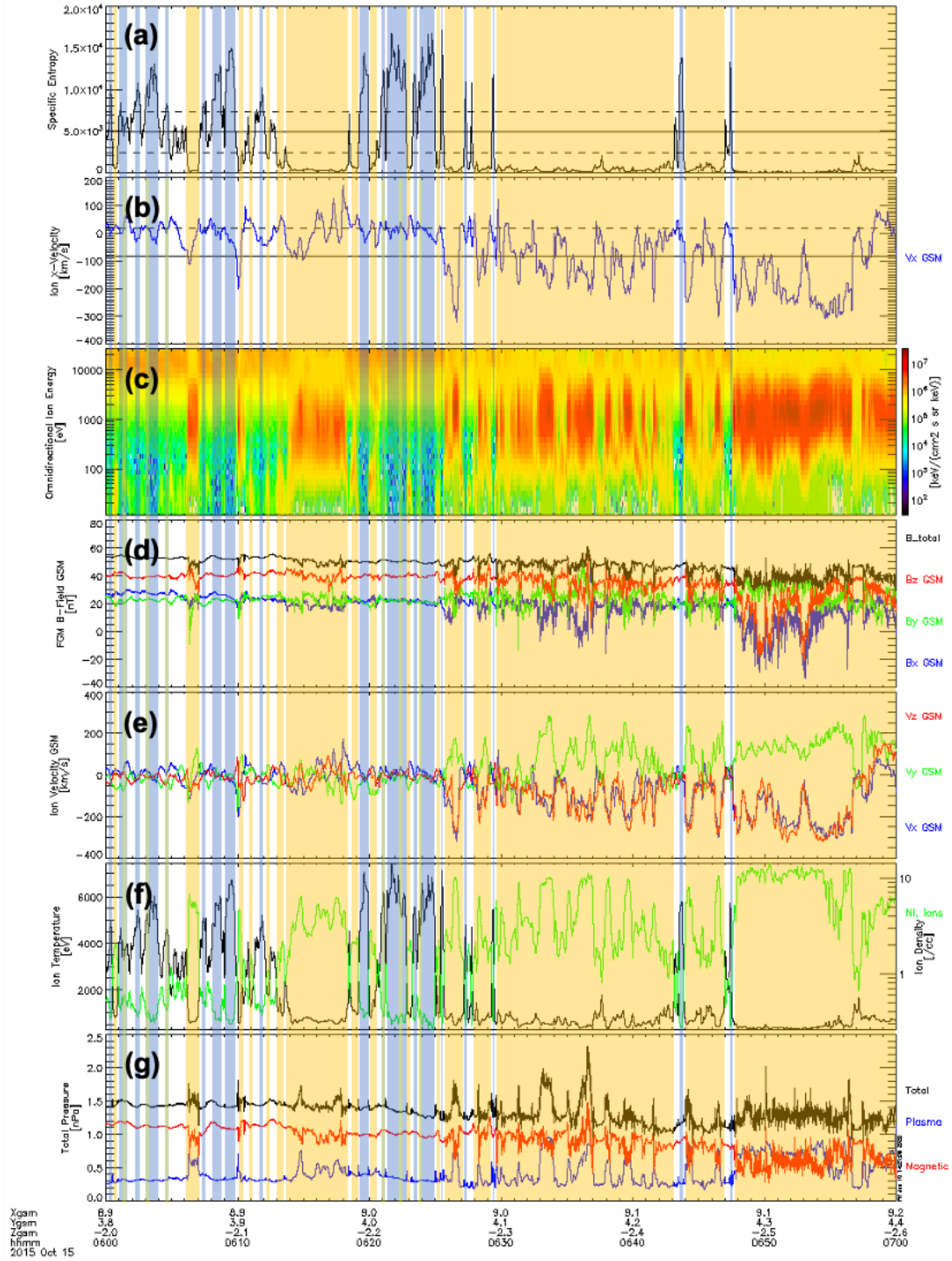
- 785 Giles, J. C. Dorelli, L. A. Avanov, W. R. Patterson, F. Plaschke, and W. Magnes
786 (2016), Observations of Large-Amplitude, Parallel, Electrostatic Waves Associated
787 with the Kelvin-Helmholtz Instability by the Magnetospheric Multiscale Mission,
788 *Geophys. Res. Lett.*, *43*, 8859–8866, doi:10.1002/2016GL070404.
- 789 Wing, S., J. R. Johnson, P. T. Newell, and C.-I. Meng (2005), Dawn-dusk asym-
790 metries, ion spectra, and sources in the northward interplanetary magnetic field
791 plasma sheet, *Journ. of Geophys. Res.*, *110*, doi:10.1029//2005JA011086.
- 792 Zhao, C., C. T. Russell, R. J. Strangeway, S. M. Petrinec, W. R. Paterson, M. Zhou,
793 B. J. Anderson, W. Baumjohann, K. R. Bromund, M. Chutter, D. Fischer,
794 G. Le, R. Nakamura, F. Plaschke, J. A. Slavin, R. B. Torbert, and H. Y. Wei
795 (2016), Force Balance at the Magnetopause Determined with MMS: Appli-
796 cation to Flux Transfer Events, *Geophys. Res. Lett.*, *43*, 11,941–11,947, doi:
797 10.1002/2016GL071568.



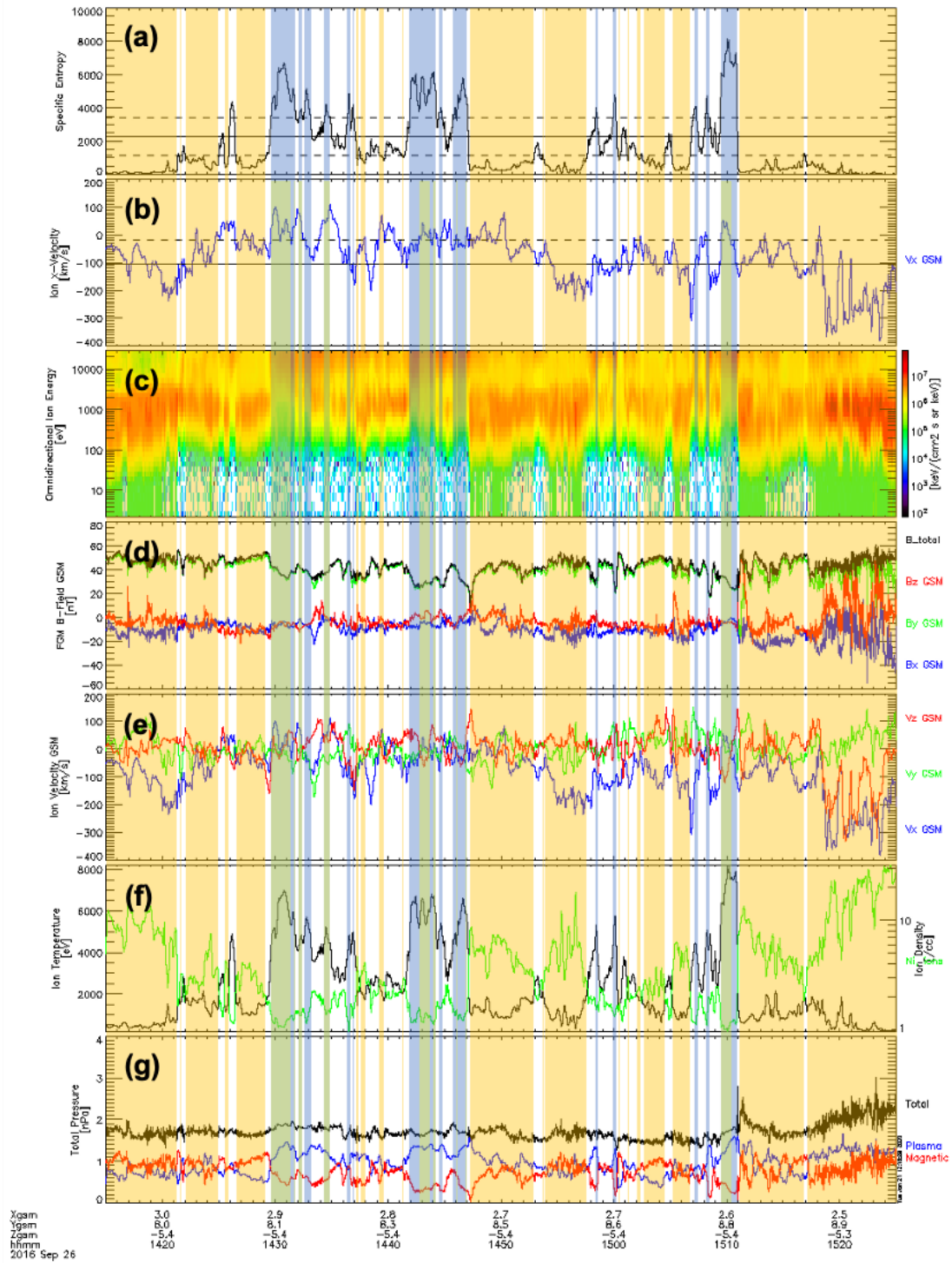
303 **Figure 5.** MMS observations of the (a) density-temperature ratio and (b) tailward velocity
 304 for the KHI event from 06:00 to 07:00 on 15 October 2015. Panels (c)-(g) are presented as in
 305 Figure 1 (a)-(e). Yellow boxes indicate magnetosheath regions, blue and green boxes are the
 306 magnetospheric regions for the velocity unconstrained and constrained methods respectively.



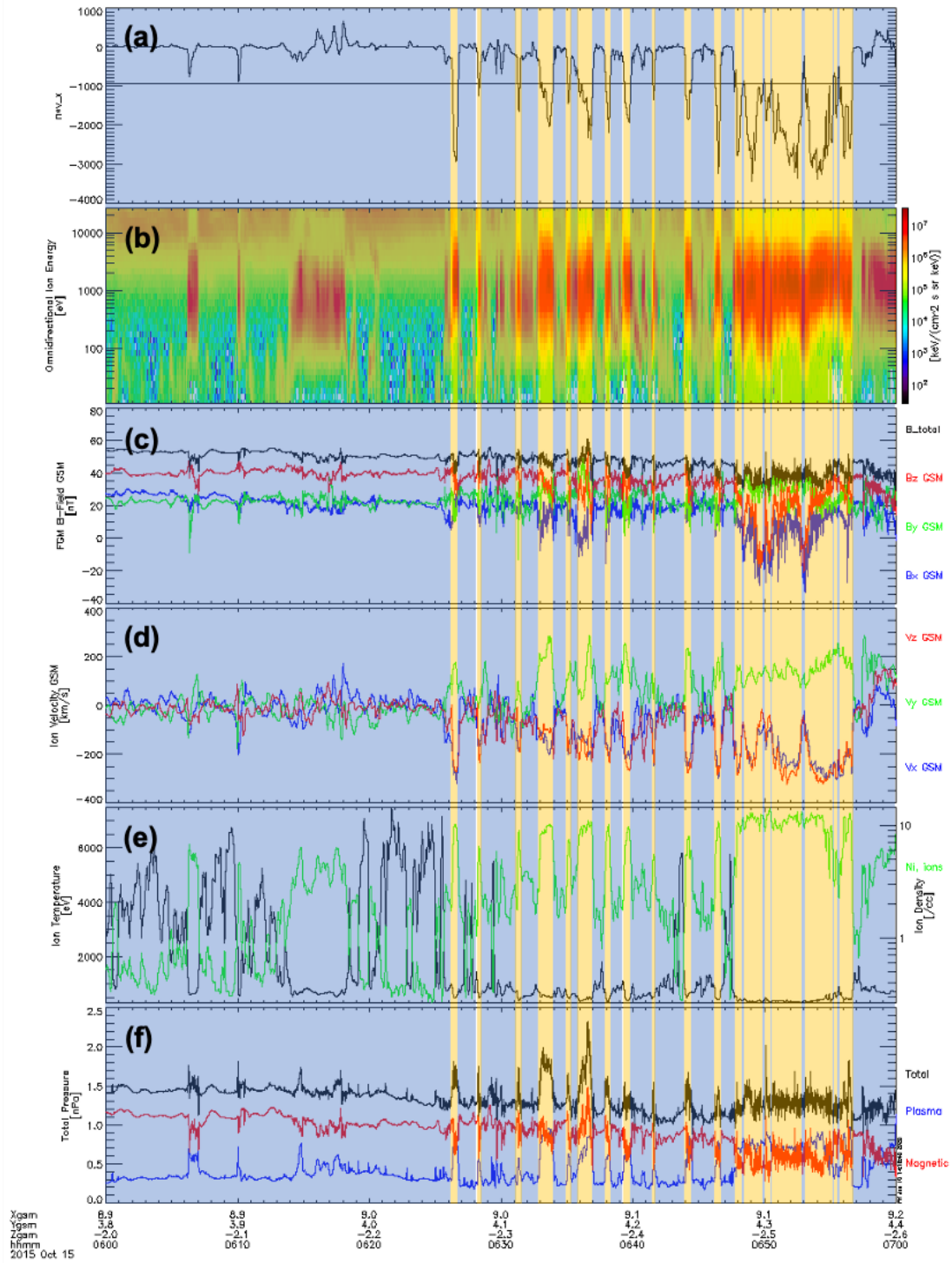
307 **Figure 6.** MMS observations, as in Figure 5 for the KHI event from 14:15 to 15:25 on 26
 308 September 2016. Yellow boxes indicate magnetosheath regions, blue and green boxes are the
 309 magnetospheric regions for the velocity unconstrained and constrained methods respectively.



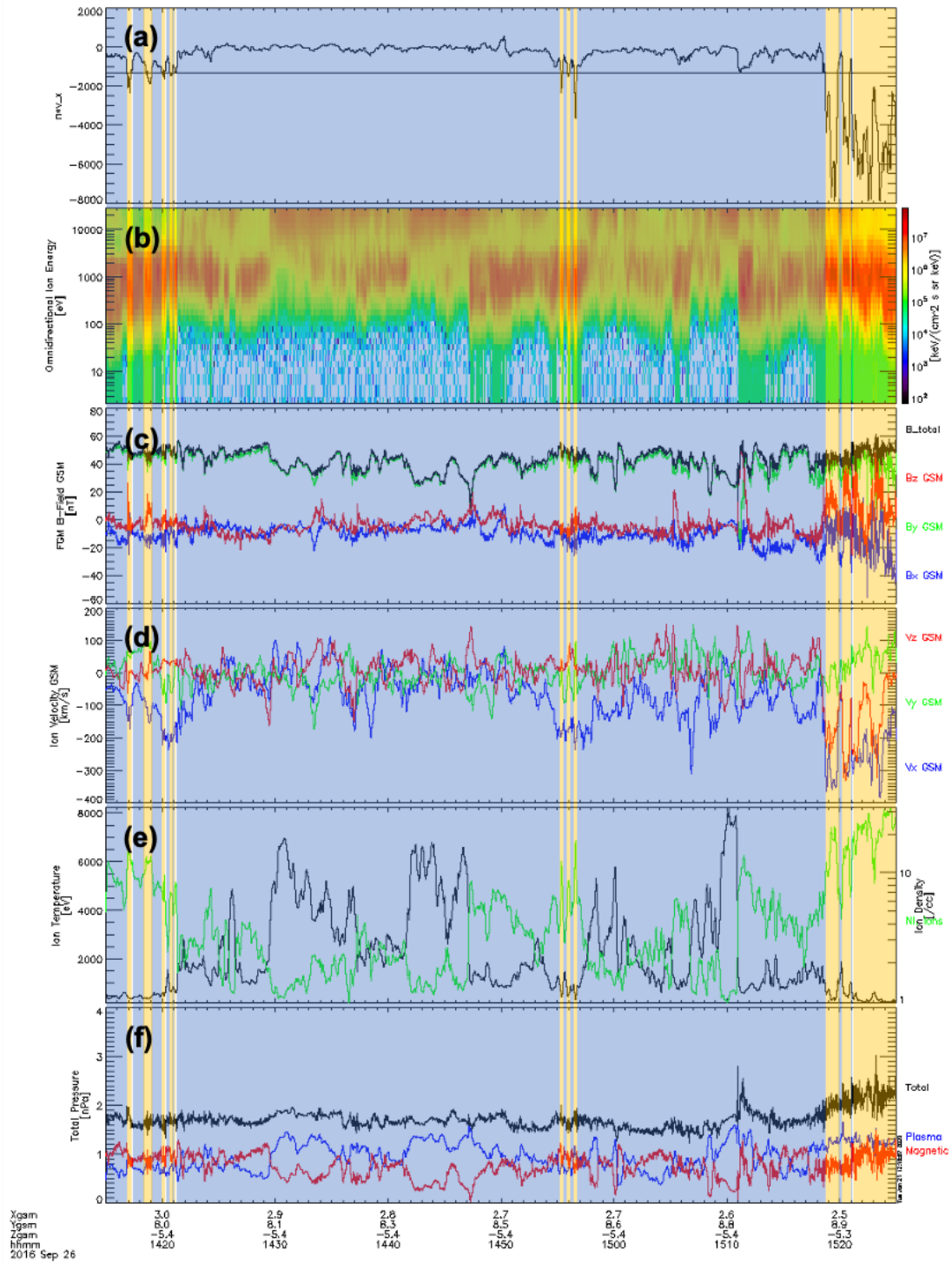
341 **Figure 7.** MMS observations of the (a) specific entropy and (b) tailward velocity for the KHI
 342 event from 06:00 to 07:00 on 15 October 2015. Panels (c)-(g) are presented as in Figure 1 (a)-
 343 (e). Yellow boxes indicate magnetosheath regions, blue and green boxes are the magnetospheric
 344 regions for the velocity unconstrained and constrained methods respectively.



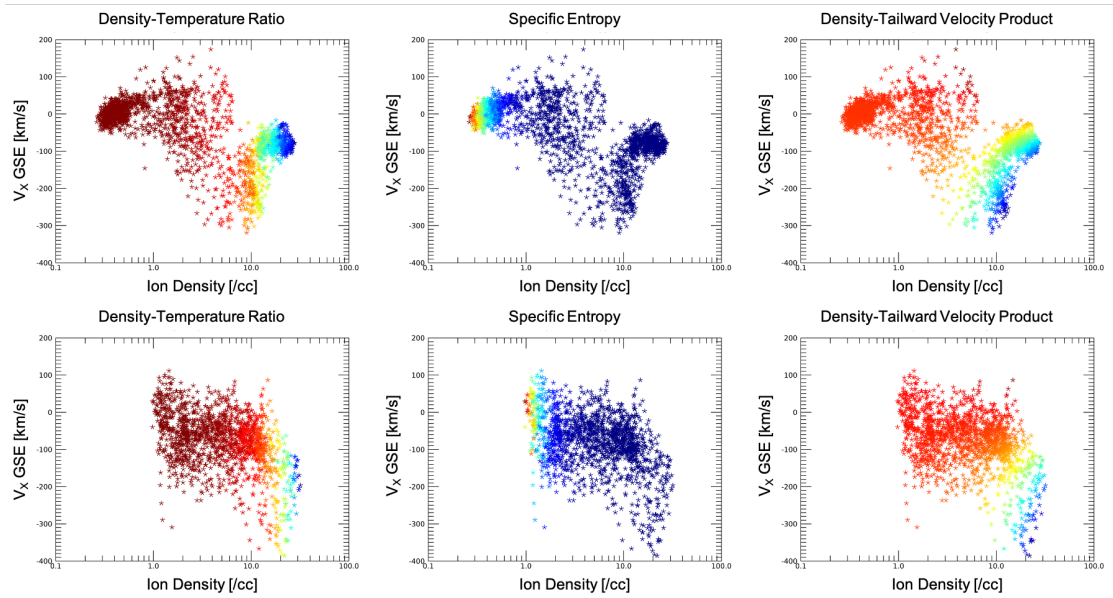
345 **Figure 8.** MMS observations as in Figure 7 for the KHI event from 14:15 to 15:25 on 26
 346 September 2016. Yellow boxes indicate magnetosheath regions, blue and green boxes are the
 347 magnetospheric regions for the velocity unconstrained and constrained methods respectively.



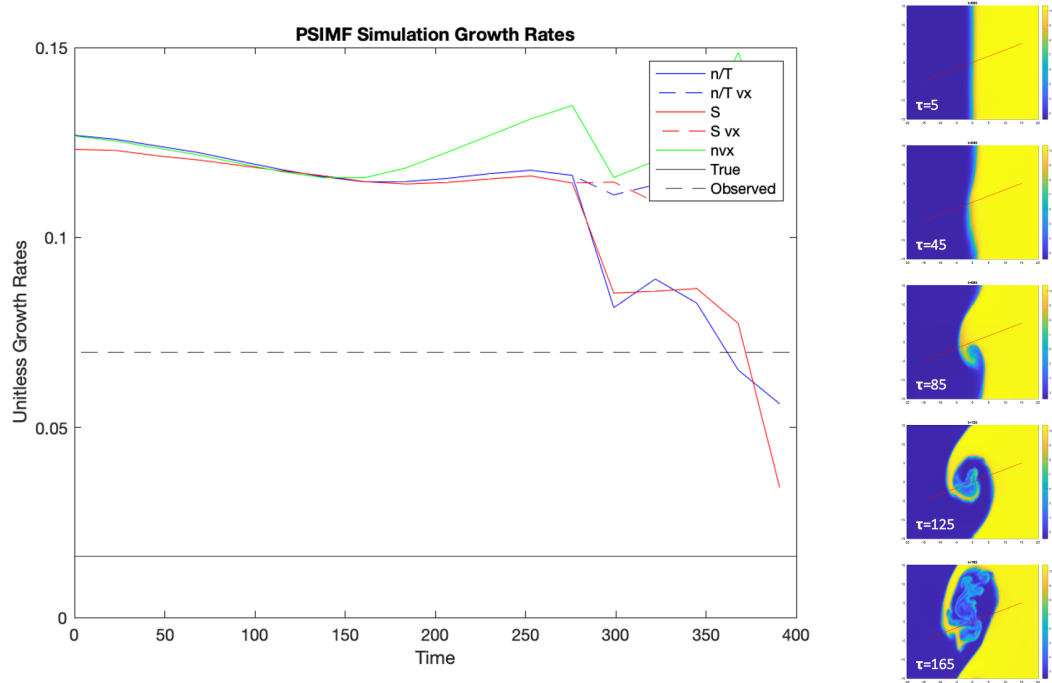
371 **Figure 9.** MMS observations of the (a) density-tailward velocity product for the KHI event
 372 from 06:00 to 07:00 on 15 October 2015. Panels (b)-(f) are presented as in Figure 1 (a)-(e).
 373 Yellow boxes indicate magnetosheath regions, blue boxes are the magnetospheric regions.



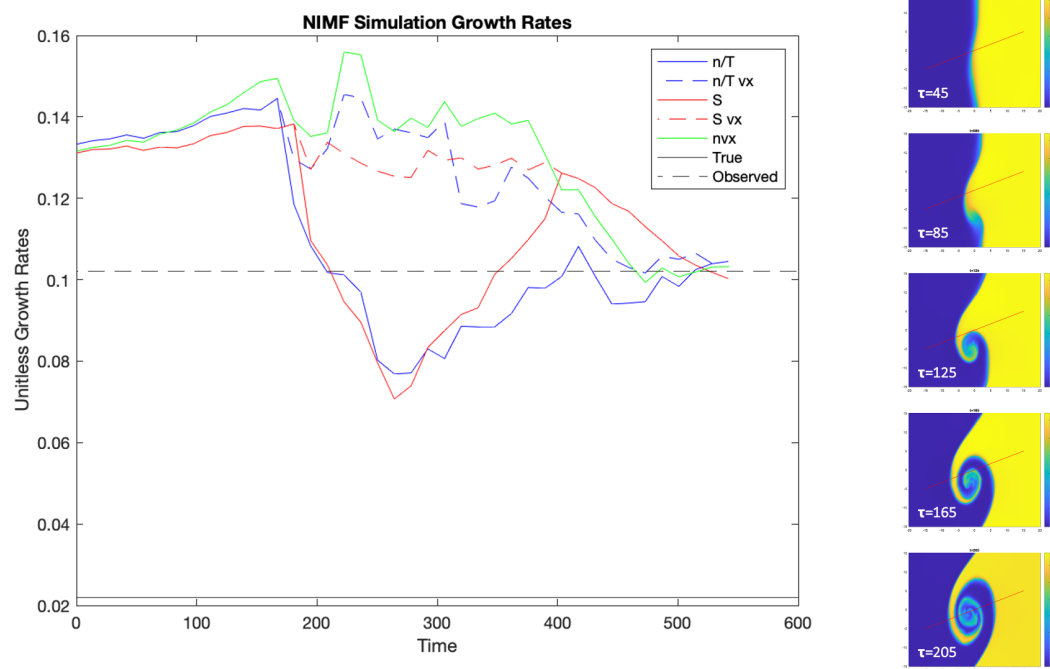
374 **Figure 10.** MMS observations as in Figure 9 for the KHI event from 14:15 to 15:25 on 26
 375 September 2016. Yellow boxes indicate magnetosheath regions, blue boxes are the magneto-
 376 spheric regions.



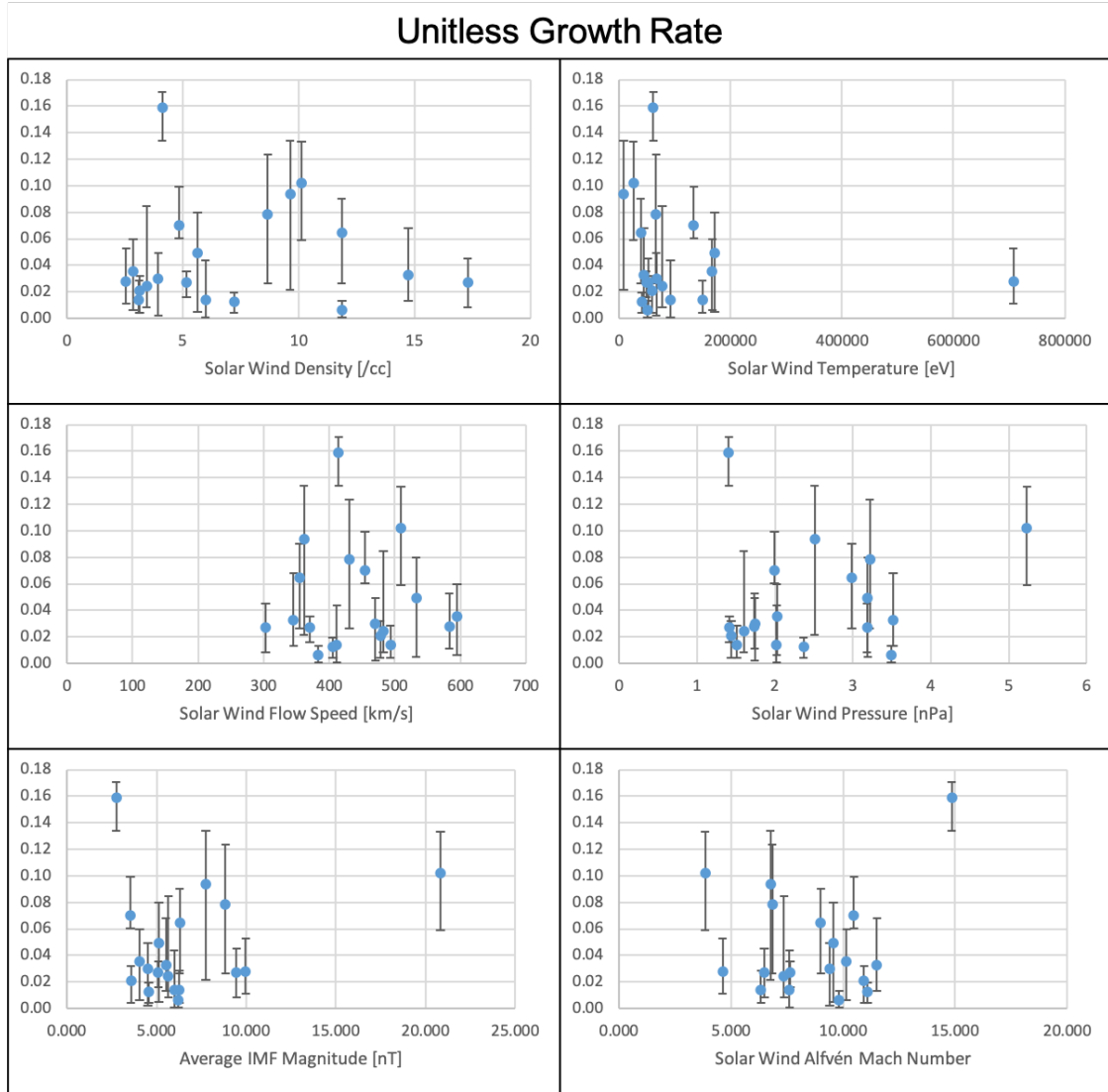
406 **Figure 11.** A comparison of MMS observed density (logarithmic scale) and tailward velocity
 407 for ions during (top) the 06:00-07:00 KH event on 15 October 2015 and (bottom) the 14:15-
 408 15:225 event on 26 September 2016. Color overlays indicate (left) density-temperature ratio,
 409 (center) specific entropy, and (right) density-tailward velocity product. Red points correspond to
 410 more sheath like characteristics and blue to more magnetosphere-like plasma.



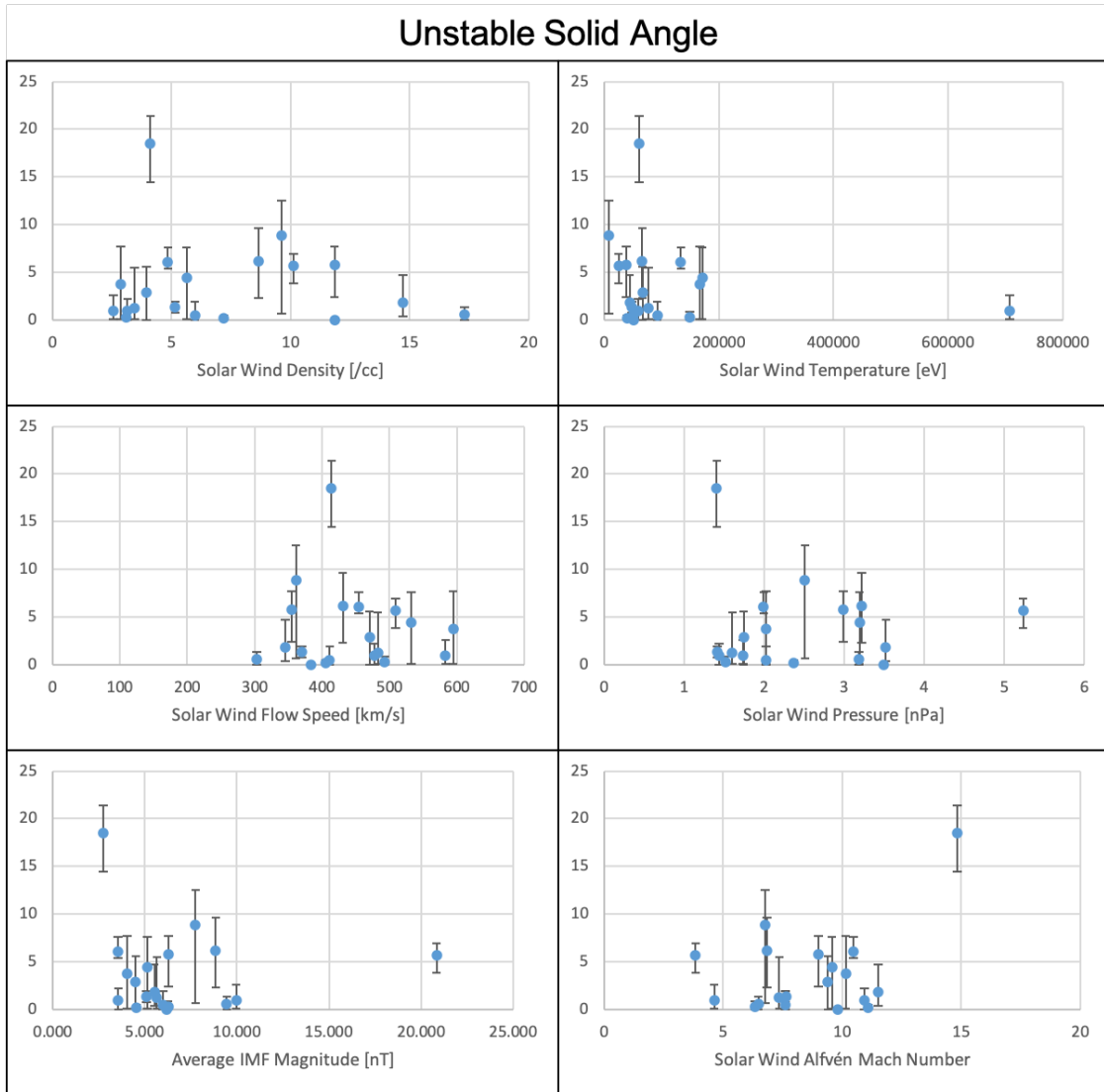
435 **Figure 12.** (Right) 2D MHD simulations of a dusk flank KHI occurring during Parker Spiral
 436 IMF. Cuts, as indicated by the red line, were taken through the instability every 10 simulation
 437 time steps and growth rates were calculated using all 5 methods and plotted as a function of time
 438 (left). The true growth rate is indicated by the solid black line. The dashed black line indicates
 439 the mean growth rate of the observational case on which the simulation is based.



440 **Figure 13.** As Figure 12 for the 2D MHD simulation of a dusk flank KHI occurring under
 441 Northward IMF.



533 **Figure 14.** Unitless growth rates as a function of solar wind (a) density, (b) temperature, (c)
 534 flow speed, (d) pressure, (e) average IMF magnitude, and (f) Alfvén Mach number. Other than
 535 the window from 300-600km/s flow speed, growth rate is independent of solar wind parameters.



552 **Figure 15.** Unstable solid angles as a function of solar wind (a) density, (b) temperature, (c)
 553 flow speed, (d) pressure, (e) average IMF magnitude, and (f) Alfvén Mach number. Other than
 554 the window from 300-600km/s flow speed, unstable angle is independent of solar wind param-
 555 eters.